

UNIVERSITY OF ANTWERP

MASTER THESIS

Diffusion of artificial self-propelled particles near boundaries

Author:
Tom CLAESSEN

Promotor:
Dr. Vyacheslav MISKO

*A thesis submitted in fulfillment of the requirements
for the degree of Master in physics*

Theory of Quantum Systems & Complex Systems (TQC)
Department of Physics

June 17, 2020

“The scariest moment is always just before you start. ”

Stephen King

UNIVERSITY OF ANTWERP

Abstract

Physics
Department of Physics

Master in physics

Diffusion of artificial self-propelled particles near boundaries

by Tom CLAESSEN

Self-propelled particles have great potential to perform tasks on a microscopic scale. Applications include the delivery, localization and pick up of micro-and nanoscopic objects as well as the on-chip chemical information processing. In order to develop these nanodevices, a better understanding of the properties of the motion of these particles in confined and crowded environments is required. Here, the behavior of self-propelled particles near boundaries is studied in more detail. In particular, the dependence of the trapping time (i.e., the time during which the motion of the particle occurs in the vicinity of the boundary) on the translational diffusion, rotational diffusion, self-propelled velocity and the dimensionality of a channel is analyzed. Further, the effect of the depletion interaction between the particles and the boundary on the trapping time near boundaries for different parameters is also studied.

Acknowledgements

I would like to sincerely thank Dr.Vyacheslav Misko for his support and advise. Whenever I had a question or had a trouble spot, he steered me in the right direction while at the same time he encouraged me to carry out my own ideas. I really enjoyed our discussions both related and not related to this thesis.

Contents

Abstract	iii
Acknowledgements	v
1 Introduction	1
1.1 Mechanisms of self-propulsion	2
1.1.1 Catalytic	2
a Self-phoresis	2
b Bubble propulsion	4
1.1.2 Light	5
a Self-thermophoresis	5
1.2 Properties of self-propelled motion	6
1.3 Guidance of self-propelled particles	10
1.4 Janus particles in channels	14
1.5 Scope and outline of the thesis	18
2 Model	19
2.1 Equations of motion	19
2.1.1 Brownian particles	19
2.1.2 Self-propelled particles	19
2.2 Mean squared displacement	20
3 Results & Discussion: Brownian particles	23
3.1 Free Brownian particles	23
3.2 Reflecting boundary	24
3.3 Sliding boundary	26
3.4 Circular confinement	27
3.5 Single-file diffusion	27
3.6 Narrow channel	29
3.6.1 Reflecting boundary	29
4 Results & Discussion: self-propelled particles	31
4.1 Free active particles	31
4.2 Sliding boundary	36
4.3 Narrow channel	38
4.3.1 Sliding boundary	38
4.3.2 Reflective boundary	40
4.3.3 Random boundary	40
4.4 Trapping time	42
4.4.1 Trapping time versus the self-propelled velocity	44
4.4.2 Trapping time as a function the rotational diffusion constant	47
4.4.3 Depletion force at the boundary	49

5 Conclusions	55
Bibliography	57

Chapter 1

Introduction

Artificial self-propelled particles (SPP), or "microswimmers" are nano- or micro-scale particles that are capable of moving autonomously in a fluidic environment. They perform a typical active Brownian motion, which can be presented as the interplay between random fluctuations and active swimming in a certain direction. Because of their similarity in behavior with biological microswimmers such as bacteria [1] and enzymes [2], they are a modern topic of interdisciplinary research between physics and biology, chemistry and material science. The experimental realization and theoretical analysis of the behavior of artificial self-propellers has been a subject of many studies in the recent years [3] and this resulted in great progress in using artificial microswimmers to deliver, localize and pick-up micro-and nanoscopic objects. This is the reason why there is significant interest in medical research: SPP's that transport cargo, e.g. drugs [4], enzymes [5], offer promising techniques for treatment of various diseases. This is possible because certain SPP's can rapidly deliver medical substances to a certain location e.g. drug carriers can be passively targeted to tumors [6] through the enhanced permeability and retention (EPR) effect [7]. In genetherapy there are also promising techniques in capturing cancer cells. Thus in Ref. [8] mAb-functionalized microengine rockets where used to isolate pancreatic cancer cells.

For other applications, well-controllable autonomously moving objects can make a strong input into the devices and systems that rely on the chemical computing and information processing. SPP's can act as a tetherless carrier of the chemical species in a channel or as a trigger of some logical operations [9].

In this section, first, a small overview of how self-propulsion can be realized is provided. Second the properties of self-propelled motion are discussed. Third, the guidance of SPP's by boundaries and channels is explained. Lastly, the scope and outline of this thesis will be presented.

1.1 Mechanisms of self-propulsion

There are various ways artificial micro-and nanoswimmers can be realized. Here, different mechanisms are described according to how their propulsion is realized. Two main types of self-propulsion can be distinguished: catalytic and light-induced propulsion.

1.1.1 Catalytic

Catalytic propulsion is made possible by conversion of chemical energy into mechanical energy resulting in a self-propelled motion in a certain direction. Important in designing this type of propulsion is the asymmetric placement of the catalyst which results in a non-uniform consumption of a suitable environment and a non-uniform distribution of the reaction products. This asymmetry will lead to the locomotion of the object.

In a biological system, catalytic propulsion is the common functional principle of self-propelling on the molecular scale: the three cytoplasmic motor classes: myosins (move on actin filaments), dyneins and kinesins (move on microtubules) all use adenosine triphosphate (ATP) hydrolysis to cause a small conformational change in a globular motor domain which will be amplified and results in movement [10].

Reactions that occur at the catalytic sites can give rise to locomotion through a number of different mechanisms that can again be divided in two groups: self-phoresis and bubble propulsion.

a Self-phoresis

Self-phoresis is the use of short-ranged interactions between colloidal particles and a local gradient. These (scalar) gradients give rise to the motion of the particle and can be realized by gradients of temperature (self-thermophoresis), electric (electrophoresis) potential, or solute concentration (self-diffusiophoresis) [11]. Self-thermophoresis is induced by light absorption of SPP's and will be discussed in subsection 1.1.2.

1 Self-diffusiophoresis

In diffusiophoresis, gradients of soluble or non gaseous reaction products induce motion of colloidal particles in a solution. The speed and direction of the motion will depend on the interaction between the particles surface and the solute and the magnitude of the solute gradient. Although in general, diffusiophoresis does not involve a catalytic process, this phenomenon can be caused by a catalytic side on a particle, i.e. the particles themselves are the source of the gradient and this process can be called self-diffusiophoresis. This is illustrated in Figure 1.1. For a spherical particle that is immersed in a solution of an uncharged solute with a certain uniform concentration gradient ∇_c far from the particle, the diffusiophoretic velocity v_d is

$$v_d = \frac{k_B T}{\eta} K L \nabla_c, \quad (1.1)$$

where k_B is Boltzmann's constant, T the absolute temperature. K and L are length scales that depend on the physical interactions between the particles and the molecules in the solution [12].

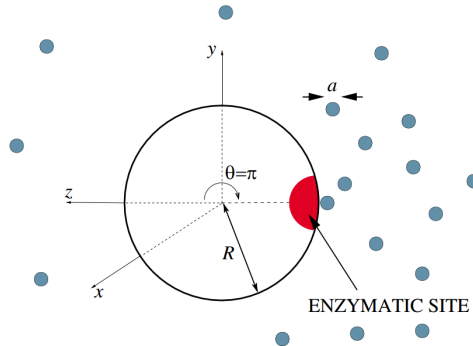


Figure 1.1: Schematic of a particle that causes a gradient by an enzymatic site which produces an asymmetric distribution of reaction products which results in a gradient. Figure taken from Ref. 1.1.

The most mathematical models of self-diffusiophoresis consider particles and the surrounding solution to be macroscopic. A constitutive model is used for reactions that happen at the enzymatic or catalytic site. It is also possible to describe this by using Brownian discrete colloidal particles to model the solute molecules.

2 Self-electrophoresis

The second type of phoresis that can be caused by a catalytic mechanism is self-electrophoresis.

Electrophoresis is the movement of a particle in an electric field. Self-electrophoresis is the movement of a particle due to its own generated electric field. Although no biological swimmers are confirmed that use this mechanism, artificial electrophoretic swimmers have been created [13][14]. The requirement for self-electrophoretic locomotion is a charged surface on a swimmer and a self-generated electric field. When the surface comes in contact with an electrolyte solution, it will acquire an electrical charge and screening layers of ions with the opposite charge (counterions) will be attracted whilst ions with the same charge will be repelled. The balance between electrostatic force and diffusion will result in a diffuse screening layer of counterions close to the surface. This diffuse layer together with the charged surface is called the electrical double layer (EDL). The thickness of this layer is called the Debye length λ_D . To describe how a field can be generated, we can use bimetallic particles as an example. Exchange of ions between the particle and the solution is caused by electrochemical reactions on the surface of the particle. If for example hydrogen peroxide is the fuel, peroxide oxidation takes place on the anode (e.g. platinum) side and on the other side peroxide reduction will take place (e.g. gold). At the anode, the oxidation reaction will produce protons while on the cathode, protons will be used for the reduction process. This way a proton, and thus a charge, gradient is produced. One can

think of the particle as an electrical dipole and a corresponding electrical field is generated. This is illustrated in figure 1.2.

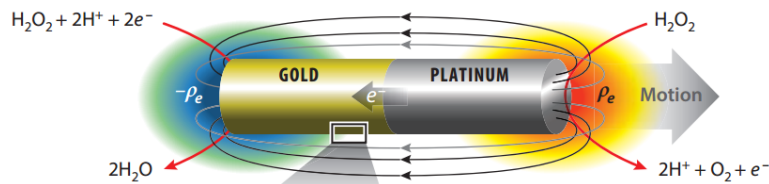


Figure 1.2: Schematic of a platinum-gold nanorod. Because of the difference in electron affinity between the two materials, electrons will conduct through the rod towards the cathode (gold) where electrons and protons are consumed in the reduction of peroxide. These reactions cause an asymmetric charge density distribution in a diffuse layer around the nanorod. An electrical field is generated as a result. Because there is a positive net charge in the electrical double layer, the electric field will exert a body force (a force throughout the body) on the nanorod. Figure taken from Ref. [15].

b Bubble propulsion

In bubble propulsion, the generation of bubbles of a gaseous reaction product will cause the self-propulsion.

An example often used in literature is presumably the first artificial engine that is based on the use of a catalyst for locomotion [16]. Here, small ($< 1\text{ cm}$) hemicylindrical plates with on one side a small area of platinum float on the surface of an aqueous solution of hydrogen peroxide. The reaction $2H_2O_2 \rightarrow O_2 + 2H_2O$, i.e. the decomposition of hydrogen peroxide catalyzed by the platinum, will generate "bubbles" that power the movement of these plates. In figure 1.3, the schematic of such a plate is showcased.

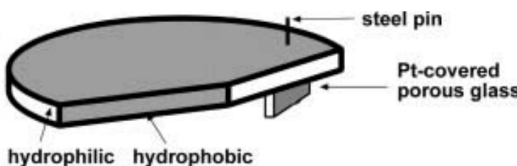


Figure 1.3: Schematic of the artificial SPP used in [16]. The Pt-covered porous glass is only covered on one side and thus there is an asymmetric placement of the catalyst which results in a non-uniform distribution of the reaction products, i.e. the bubbles. Figure adapted from Ref. [16].

1.1.2 Light

In the section above, it was shown how catalytic reactions placed in an asymmetrical fashion on an artificial particle can lead to self-propelling motion. The downside of this technique is that in order to sustain constant activation of the particle, fuel needs to be decomposed, e.g. hydrogen peroxide is catalyzed via platinum. This way, the activation of the particle depends on the limitation of the supply of fuel. To avoid this problem, it has been shown that light can be used to cause self-propelling motion via thermophoresis.

a Self-thermophoresis

Self-thermophoretic microswimmers have been realized by using gold-capped Janus particles in water [17]. Here, laser light absorbed by the gold caps, that is coated on one hemisphere, causes a local temperature gradient along which the Janus particles move. Descriptions of this behavior can be found in [18] and [19]. Figure 1.4 illustrates an example of an experiment of self-thermophoresis. $1\mu\text{m}$ Au-silica Janus particles are placed in a chamber at a low concentration and are, after applying a laser, pushed to the upper surface of the chamber and move around within the laser irradiated region.

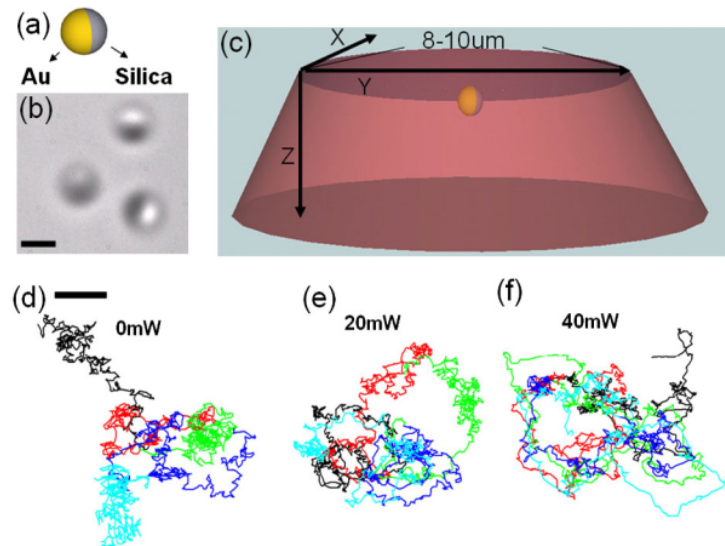


Figure 1.4: (a) Schematic of Janus particles, (b) bright field image under a microscope, the dark sides of the particles are the Au coatings. (c) Schematic of a Janus particle in a chamber. The red cone is the laser which is directed in the z-direction, starting from the bottom. (d) to (f) The trajectories of a Janus particle in the XY plane. The different colors correspond with different time intervals (2 s). (d) No laser irradiation. (e) 20mW, Brownian motion becomes more active Brownian motion. (f) 40 mW, some segments of the trajectory show very little noise, active Brownian motion is more pronounced. Figure taken from Ref. [17].

The direction of the motion of the Janus particles in Figure 1.4 is determined by the polarity of the Janus particles in contrast to phoretic motion guided by external fields which in some regards increases the autonomously of the SPP's. However, still complete autonomy is hindered by need for the use of a laser.

1.2 Properties of self-propelled motion

A framework for theoretical modeling of self-propelled particles is provided by the traditional Langevin theory of a particle with translational and orientational diffusion including an effective external force. The motion of micro-swimmers is force-free: this motion, however, can be described by the Langevin equations with an effective force which describes the propulsion mechanism on average [20]. This will be explained a bit further.

The Langevin theory and equations where originally used to describe Brownian motion. This type of motion is named after the botanist Robert Brown who first described this phenomenon in 1828. He looked at seeds inside pollen grain in water and noticed the particles moving irregular through water. It was only much later that the mechanisms of this movement were explained by Albert Einstein in a paper in 1905. He explained very precise that the motion observed by Brown is the result of the pollen interacting with individual water molecules. After experimental confirmation of Einstein's predictions, the existence of atoms and molecules was verified. This resulted in the Nobel prize in physics in 1926. Since this Brownian motion is the results of micron size particles immersed in a fluidic environment, an adapted version of the equation that describes this motion, i.e. the original Langevin equation, is well suited to describe artificial self-propelling particles suspended in a fluid.

When dealing with spherical particles that have one orientational degree of freedom, the Langevin equations are given by:

$$\frac{d\mathbf{r}}{dt} = \beta D[\mathbf{F}\hat{\mathbf{u}} - \nabla U + \mathbf{f}], \quad (1.2)$$

$$\frac{d\phi}{dt} = \beta D_{rot} \mathbf{g} \cdot \hat{\mathbf{e}_z}, \quad (1.3)$$

where $\mathbf{f}(t)$ and $\mathbf{g}(t)$ are the Gaussian white noise random force and torque, respectively. They are characterized by $\langle f_i(t) \rangle = 0$, $\langle f_i(t)f_j(t') \rangle = 2\delta_{ij}\delta(t-t')/\beta^2 D$, $\langle g_i(t) \rangle = 0$, $\langle g_i(t)g_j(t') \rangle = 2\delta_{ij}\delta(t-t')/\beta^2 D_{rot}$. The indices i and j refer to the respective components, δ_{ij} is the Kronecker delta and $\langle \dots \rangle$ is a notation for the noise average. $U(\mathbf{r})$ is an external potential that is included in the equation for the sake of generality, but in this thesis it will be set to zero. β Is the effective thermal energy: $\beta = (k_B T)^{-1}$, and herein k_B and T being Boltzmann's constant and the temperature, respectively . D and D_{rot} are the translational and rotational diffusion constant, respectively. $\mathbf{F} = F\hat{\mathbf{u}}$ is the driving force of the self-propelled particles.

When dealing with spherical SPP's in two dimensions, the motion of the particle can be described by the center -of-mass position vector $\mathbf{r}(t) = (x, y)$ and the angle ϕ between $\hat{\mathbf{e}}_x$ and $\hat{\mathbf{u}} = (\cos(\phi), \sin(\phi))$, this is depicted in Figure 1.5. These equations also express an overdamped regime: a friction term is missing. Most systems with self-propelled particles are described by this regime although there are examples of modeling self-propelled particles with a Rayleigh friction term [21]. In this thesis an overdamped regime will be assumed and thus equations (1.2) and (1.3) or adaptations of those equations can be used.

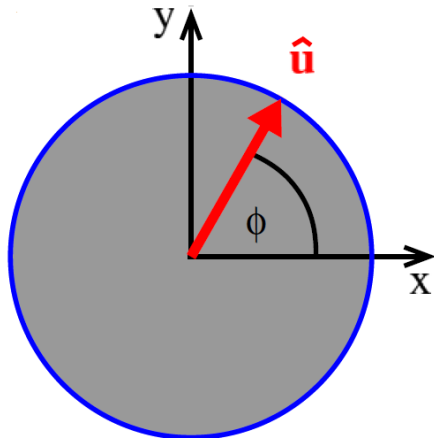


Figure 1.5: Schematic of a 2D self-propelling particle. $\hat{\mathbf{u}}$ Is the direction vector of the self-propelled motion. Figure taken from Ref. [21].

Self-propelled particles can display two main types of motion: persistent motion and directed motion depending on the system. Directed motion occurs when self-propelled particles are driven by an external field, e.g. magnetic particles guided by a magnetic field, single cells can be directed by external signals. In this thesis however, persistent motion will be studied. This type of motion has been described by a class of stochastic processes that are known as persistent random walks. Here, the direction of motion changes, but on shorter time scales, there will be a persistence to move in a certain direction. This is also apparent from equations (1.2) and (1.3) that are used to describe this motion. To characterize this behavior, the mean squared displacement (MSD) is calculated. It indicates the deviation between the position of a particle and some reference position over time t . This statistical tool is often used in literature for describing diffusion processes such as Brownian motion. In chapter 2, it is explained how the MSD is calculated in this thesis. Here, only the theoretical calculated MSD and experimental found MSD for persistent motion are described. The MSD for particles that only perform a Brownian motion is well-known: $MSD(t)=2dDt$. Where d is the dimension of space and D the translational diffusion constant. For active particles, it is known that the velocity autocorrelation function for persistent motion shows a finite decay time, i.e. given a time t , one can find a finite Δt so that the autocorrelation function: $=\langle \mathbf{v}(t) \cdot \mathbf{v}(0) \rangle$ becomes zero (uncorrelated) for short times. This property gives rise to a so-called ballistic regime. A ballistic regime is characterized by a certain time interval where the MSD is proportional

to t^2 : $\text{MSD} \propto t^2$. For longer times, a crossover to a diffusive regime takes place, characterized by a MSD proportional to t : $\text{MSD} \propto t$. In Ref. [22] an equation for the MSD of a spherical particle performing a persistent walk was derived:

$$\langle x^2(t) \rangle = \frac{2\langle v \rangle^2}{\kappa^2} (\kappa t - 1 + e^{-\kappa t}) + 2 \frac{\langle v^2 \rangle - \langle v \rangle^2}{(\kappa + \beta)^2} ((\kappa + \beta)t - 1 + e^{-(\kappa+\beta)t}), \quad (1.4)$$

κ is the translational diffusion constant. This equation will reduce to the well known result for persistent Brownian particles when there are no speed fluctuations: $\sigma^2 = \langle v^2 \rangle - \langle v \rangle^2 = 0$. The crossover regime in absence of those fluctuations occur at $t \sim \kappa^{-1}$. When fluctuations become relevant, the crossover occurs at $t \sim (\kappa + \beta)^{-1}$. From equation (1.4) different regimes can be found by changing certain variables. In Ref. [22] 4 regimes are described depending on the scaled speed variance $\mu = \sigma/\kappa$ and the diffusion time $\gamma = \beta/\kappa$. The MSD $\xi = x/(\kappa\langle v \rangle)$ and the time $\tau = \kappa t$ are also made non-dimensional. In Figure 1.6 the different regimes are depicted. The red line illustrates a MSD where $\mu = 0$. There is only one regime here: $\text{MSD} \sim \tau^2$. The other curves all have $\mu = 100$, here γ is changed. For $\gamma \ll 1$ there is a single crossover at $\tau \sim 1$, displayed by the dashed green line in Figure 1.6. Larger values of γ solutions are found that lie between the green line and the solid red line. A more complex succession of regimes can be observed when γ is large enough ($\gamma = 10^6$), this is illustrated by the solid black line in Figure 1.6.

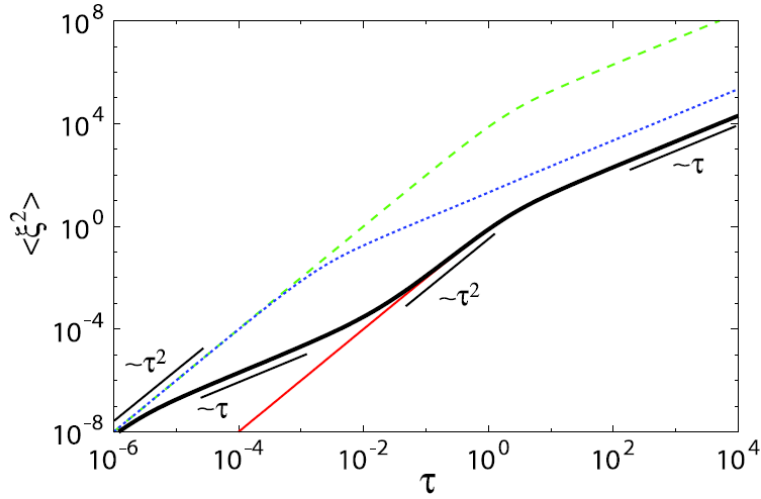


Figure 1.6: Scaled mean squared displacement as a function of scaled time for persistent walks. The different curves are calculated from equation (1.4). The red line corresponds to a persistent walk without speed fluctuations, for the other curves, the fluctuations are $\mu = 100$. The dashed green line corresponds with $\gamma = 10^{-3}$. The dashed blue line corresponds with $\gamma = 10^3$. Figure taken from Ref. [22]

Experimentally, super-diffusive regimes have been found for short times. In Ref. [23] the MSD of polystyrene spheres with a coating of platinum immersed in hydrogen peroxide are studied for different concentrations of hydrogen peroxide. The results are given in Figure 1.7, the black line illustrates the MSD of these particles without fuel. The MSD is proportional to t , which indicates normal Brownian motion. When the concentration of hydrogen peroxide is increased, a super diffusive regime can be observed, i.e. $\text{MSD} \propto t^\alpha$, $\alpha > 1$ for short times (most clear for the purple, blue and green curves in Figure 1.7). For longer times, the MSD becomes proportional to t , but with a substantially enhanced diffusion constant.

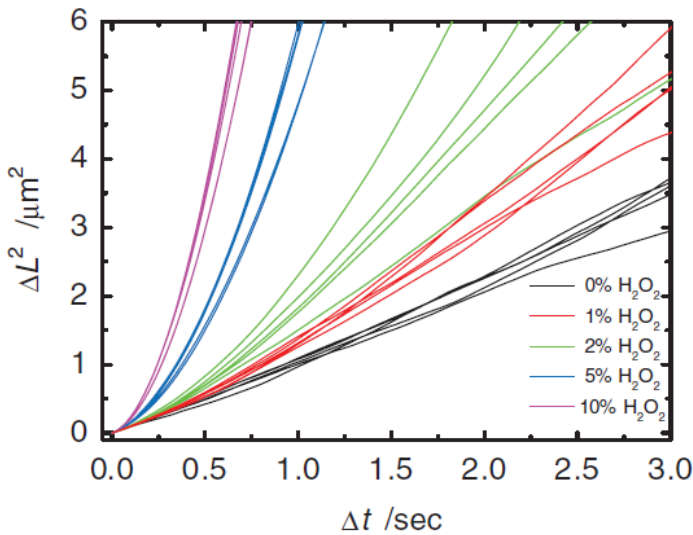


Figure 1.7: Mean squared displacement for Pt-coated sphere trajectories. Different colors correspond to different concentrations of hydrogen peroxide. Higher concentrations give rise to super-diffusive behavior for short times. Figure taken from Ref. [23].

Another example of a super-diffusive regime for early times can be found in Ref. [17]. Here, self-propelled motion is caused by self-thermophoresis via absorption of a laser. For higher laser power (especially the pink curve), a clear super-diffusive regime can be seen. In figure 1.8, the results are showcased. Similar to the results in Figure 1.7, a super diffusive regime for short times and for a high self-propelling component is found, as well as an enhanced diffusion constant for longer times.

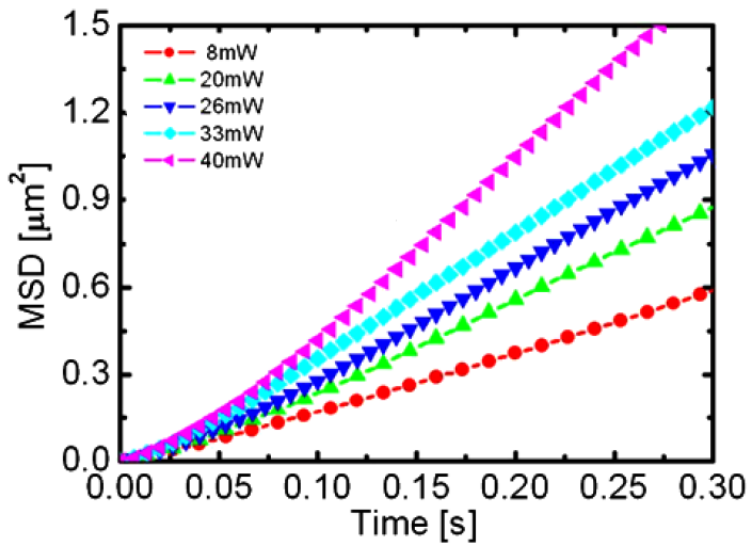


Figure 1.8: Mean squared displacement for self-thermophoretic Janus particles. Different colors correspond to different laser power. Higher laser power result in a observable super-diffusive regime for short times. Figure adapted from Ref. [17].

1.3 Guidance of self-propelled particles

The ability to accurately steer SPP's is of course essential for applications mentioned above (cargo transportation, repair and drug delivery). The major barrier is Brownian motion that will randomize the orientation of the particles and will thus lead to long time isotropic enhanced diffusion.

In order to gain control over the direction of the motion of the microswimmer, several methods of guiding this motion where already described: self-phoresis, light-induced propulsion, bubble propulsion,... There lies still great difficulty in creating and maintaining the chemical gradients and the spatial precision in methods that use spatial gradients. Also, the precision of this types of guidance remains rather poor. While methods that use magnetic guidance, e.g. a magnetic field and particles with a magnetic coating, have proven to be more precise and can be employed easily for tubular particles, for spherical colloids however, sophisticated engineering of the multilayer coating is required and complex external apparatus are required for guiding individual particles. [24][25]. This is illustrated in Figure 1.9.

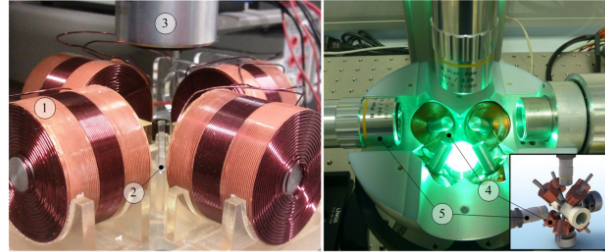


Figure 1.9: Electromagnetic systems control the motion of Janus particles in 2D and in 3D. This figure is to illustrate that a complex external apparatus is needed to guide individual Janus particles. The advantages of autonomous motion and operation of Janus particles is partly hindered in using such a machine. Figure taken from Ref. [25]

In Ref. [26] & [27] it has been shown that an external magnetic field can be used to obtain a deterministic motion of catalytic engine and to efficiently control the velocity and orientation (deterministic motion in opposite direction is possible) of those particles. Their experimental setup is schematically illustrated in Figure 1.10.

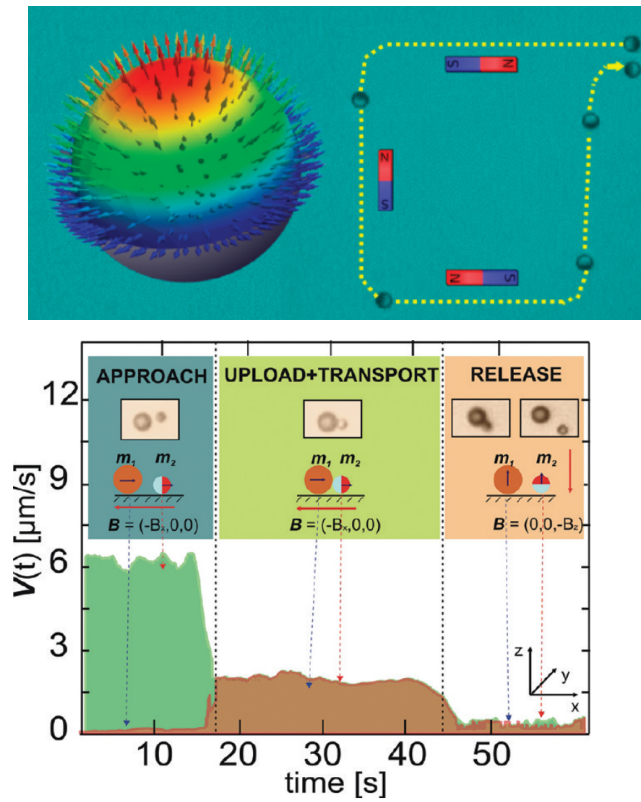


Figure 1.10: Top: schematic of a janus particle following a path directed by external magnetic field. Bottom: targeted delivery of a superparamagnetic cargo particle. time evolution of the velocity of a Janus particle and a Janus particle with a cargo. By changing the orientation of the magnetic field, the cargo is released. Figures taken from Ref. [26].

Other strategies for directing microswimmers like electrophoretic trapping [28] and using gravity [29] have been investigated, but like it was the case for magnetic guidance, they also lack autonomy or can (in the case of gravity) only constrain along one-dimension. Because of these reasons a natural and rather easy to implement guidance can be provided by boundaries. In general, because of the low density of artificial microswimmers compared to the solution in which they move, they tend to sediment and move near surfaces (and thus boundaries). This has of course a great impact on the trajectories of the swimmers. A first example of this impact is that theoretical, microswimmers with long range hydrodynamic interactions between microswimmers and nearby surfaces give rise to a circular motion or a trapping at the boundary [30]. An example of an experiment displaying the importance and effect of boundaries can be found in Ref. [31]. They examined behavior of active microswimmers in an environment with topographical structures like a straight wall, a pore and periodically arranged obstacles. In the encounter with the wall, the particle slides along the wall after making contact with the wall and slides along this wall until rotational diffusion realigns the particle such that the orientation is away from the wall and the particle detaches, this process is depicted in Figure 1.11. They measured the distribution of the wall trapping time t_{trap} and found good agreement with numerical simulations and that the average contact time t_{trap} is a lot smaller than the average rotational diffusion time $t_{rot} = \frac{1}{D_{rot}}$: $t_{trap} \ll t_{rot}$. This is due to the angular distribution of incoming particles. It is important, because it suggests that the rotational diffusion remains largely unaffected by the encounter with the wall. When active particles were confined in a pore, i.e. a circular confinement, they found that when the self-propelling velocity was low, the pores were explored in a uniform fashion and resemble that of a non-active Brownian particle. When the velocity was increased, via changing the illumination intensities, the ballistic length becomes larger and the chance of finding a particle near the confinement wall becomes greater. When the particle touches the wall, it will diffuse along the wall until the rotational diffusion orients the cap towards the interior. This process is depicted in Figure 1.12.

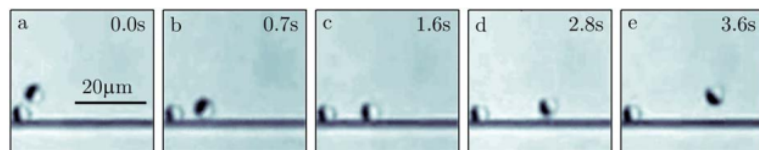


Figure 1.11: Encounter between a microswimmer (upper particles going the the right in the picture) and a wall. (a) Approach of the wall. (b) Contact with the wall. (c) sliding on the wall. (d-e) detachment from the wall. Figure taken from Ref. [31]

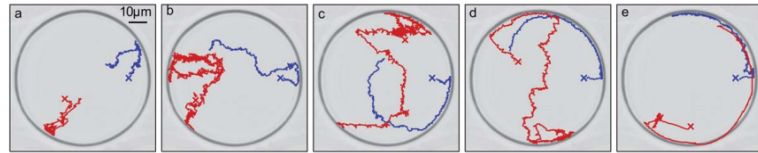


Figure 1.12: Microswimmer in a circular confinement. The red lines are measured trajectories, the blue are simulated trajectories. As the illumination intensity increases from (a) to (e), the particles reside longer near the confinement. All these trajectories are sampled over the same time. Figure taken from Ref. [31]

Further, it has been shown that geometric boundaries can help steer Janus particles. [32] They managed to produce directed motion of catalytic motors when moving in close proximity to solid surfaces. This is achieved through active quenching of the Brownian rotation by constraining it in a rotational well, caused not by equilibrium but by hydrodynamic effects. Figure 1.13 shows particles that are moving along geometric boundaries at speeds of up to $10 \mu\text{ms}^{-2}$

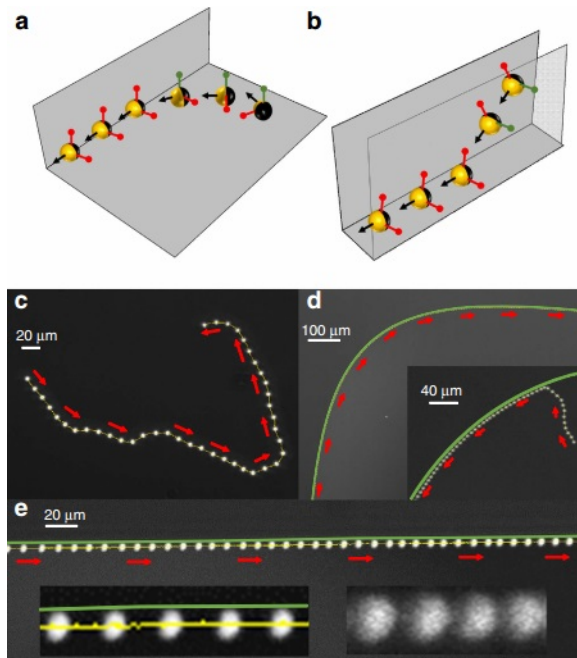


Figure 1.13: (a),(e) schematics of Janus particles that encounter multi-planar geometries. The red axis indicate forbidden rotations that are due to proximity to a plane, the green axis are the allowed rotations.(c)-(d) Overlaid still frames from fluorescence microscopy videos with equal time gaps. The yellow line shows the complete trajectory, the green line shows the location of vertical cuvette walls, the red arrows indicate the direction of motion. (c) Free particle. (d) Moving along the curved edge of a glass cuvette. The inset shows a colloid reaching the boundary. (e) Janus colloid moving along the straight edge of a glass cuvette. Left inset: magnified region, right inset: 'stuck' agglomerate formed at the boundary. Figure adapted from Ref. [32].

1.4 Janus particles in channels

Another growing topic in guidance of microswimmers is the transportation of colloidal particles inside narrow channels. An understanding in this type of transportation can lead to a deeper understanding of several biological systems like ion-channels, blood-vessels [33] [34], DNA manipulations and separations [35]. There is also potential in applications of micro - and nanodevices [36].

Rectification of microswimmers has been investigated in order to obtain a net particle transport on a periodic substrate in absence of external biases. In order to realize this, one needs a spatial asymmetry of the substrate and a time correlation of the non-equilibrium fluctuations (Pierre Curie's conjecture) that are random or deterministic applied to the particles. Each particle is assumed to interact with the substrate via a periodic potential (ratchet potential). Brownian diffusion in a narrow corrugated channel can also be rectified. This is because the constituents of a mixture of repelling particles are pressed against the walls of the periodical modulated channel and their dynamics will become dependent on the asymmetry of the channel compartments, this is called a collective geometric ratchet. It is also shown that rectification of mixtures of repelling particles in an asymmetric channel can also be realized by time-correlated thermal fluctuations, like in thermal ratchets. These thermal ratchets are in general weaker than collective ratchets and collective ratchets perform less than potential ratchets. In Ref. [37] it is numerically shown that ratcheting of active Janus particles can be orders of magnitude stronger than normal thermal potential ratchets, even if just a small fraction of the particles are Janus particles. In this system, the diffusing particles utilize the kinetic energy from their environment without the need of an external field. Transport is a consequence of an autonomous symmetry-directed particle flow.

Also in Ref. [37], the rectification of a 2D asymmetric channel was simulated. The compartments of the channel were taken triangular in shape and the particles where at the boundary elastically reflected both with the self-propelled orientation angle θ unchanged and randomized. When θ was kept the same, the particles滑ed along the boundaries for an average time of τ_θ , until rotational noise $\xi_\theta(t)$ redirects the particles towards the interior of the compartment. For randomized boundary conditions, the particles will diffuse away from the boundary and the rectification effect was found to be weakened. The inset in the bottom right corner of Figure 1.14 shows the accumulation of the stationary particle probability density $P(x,y)$ along the boundaries. The inset of this figure, shows one such triangular compartment, when more of these are connected, a net directional flow of particles can be realized.

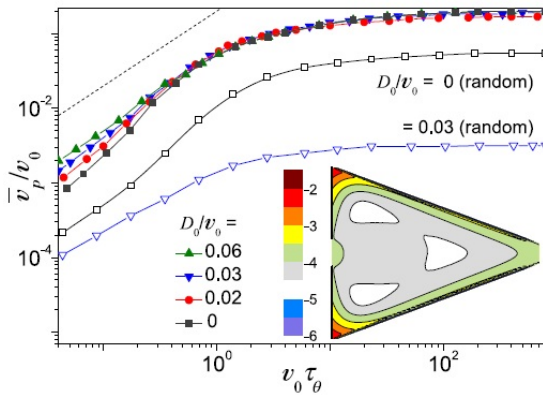


Figure 1.14: Rectification of a single point like Janus particle with a self-propulsion speed v_0 in a triangular channel. The curves are the average velocity in function of the rotational diffusion time denoted by τ_θ for a certain channel pore size and different translational diffusion constants D_0 . The open symbols represent randomized boundary conditions, the closed symbols represent sliding boundary conditions. In the upper left corner, a dashed line with slope 1 is drawn. The Inset is a (logarithmic) contour plot of the stationary probability density. Figure taken from Ref. [37].

Another example of the manipulation of self-propelled "particles" by geometric confinement can be found in Ref. [38]. Here spermatozoa were homogeneously distributed in a chamber divided by two rows of asymmetric V-shaped obstacles, shown in Figure 1.15 (a). The cells are guided by the walls and the asymmetric shape of the funnels gives rise to a higher population density in the lower chamber. Unfortunately, their design leads to cell directioning, but not as efficient as they expected. This was due to unwanted cell concentration near the convex angles of the V-shaped obstacles: Figures 1.15 (a)-(c). This makes rendering V-shaped structures less suitable for uniform sperm cell directioning and separation. The accumulation of sperm cells that are observed near the V-shaped corners and all the other corners in the chamber is a direct consequence of their persistent progressive forward movement. They solved this problem by using numerically studying the trapping-detraping transition that occurs when the curvature radius is changed. The numerical results are shown in Figure 1.16.

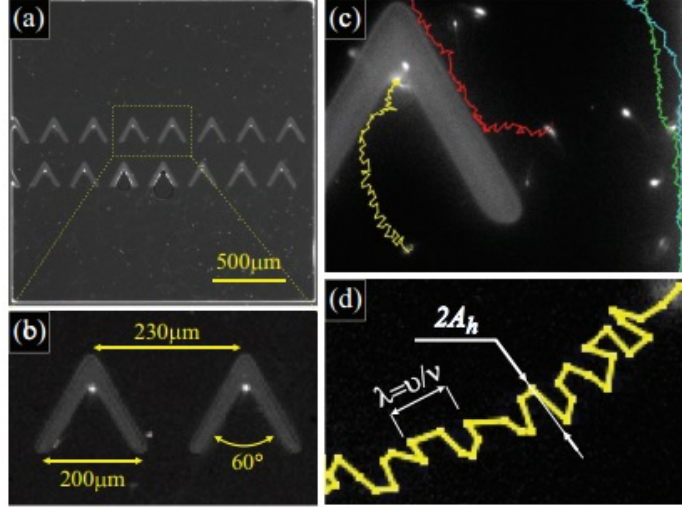


Figure 1.15: Human sperm trapping near the apices of a V-shaped ratchet **(a)** Chamber with a double row of V-shaped obstacles. A clear accumulation at all apices can be found. **(b)** Geometrical parameters and a detail of the sperm accumulation, shown by the brighter dots at the apices. **(c)** High magnification details of the behavior of the sperm cells. **(d)** Oscillation of the cell head: the amplitude is indicated by A_h and the wavelength by $\lambda = v/\nu$. Figure taken from Ref. [38].

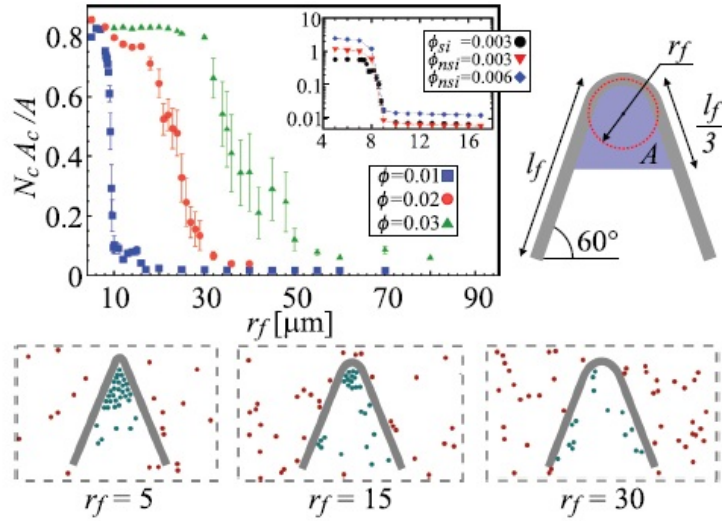


Figure 1.16: Numerical results of the obstacle curvature effects. Top left: fraction of the shaded area A (that is illustrated in the top right figure) occupied by sperm cells vs the radius of curvature for different sperm densities ϕ and a constant length of the channel l_f . The inset of the top right figure show results for lower ϕ . N_c is the average number of cells found in A . Figure taken from Ref. [38].

Lastly, it is shown that a single active Janus particle, being self-embedded in a cluster of passive particles, can unclog a channel that is filled with passive particles [9]. Figure 1.17 shows the experimental images and Figure 1.18 shows the simulated results.

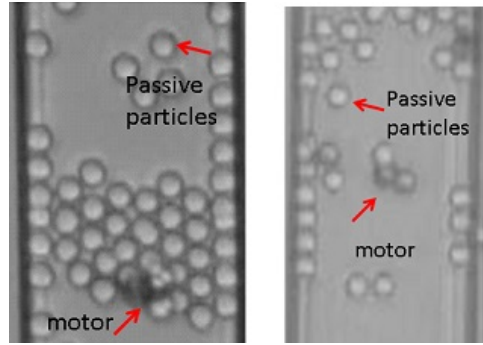


Figure 1.17: Two narrow channels with different particle densities. The dark particle is the active Janus particle, while the light particles are the passive particles. Figure taken from Ref. [9].

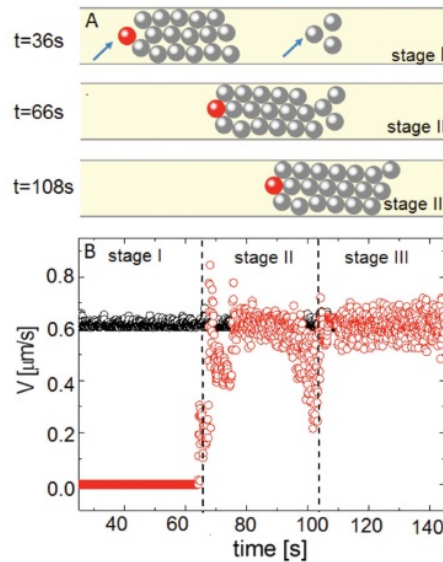


Figure 1.18: Unclogging of a channel filled with passive particles by an active Janus particle. (A) Snapshots of the particle distribution where made before the collision of the moving aggregate of the Janus swimmer (red circle in (A)) and 16 passive particles (grey circles in (A)) with three un-moving particles ($t=36$ s), at the moment of collision ($t=66$ s) and when moving as a whole cluster ($t=108$ s). (B) The corresponding velocities of the moving aggregate driven by the Janus swimmer (black diamonds) and passive particles (red open circles). Figure taken from Ref. [9]

1.5 Scope and outline of the thesis

This thesis aims to reach understanding of the behavior of active particles near boundaries. In particular, the residence of particles near boundaries as a function of different parameters such as the translational-and rotational diffusion constant, the dimensionality of the geometric confinement and the self-propelled velocity, will be studied. In order to obtain reliable results, a good agreement of the simulated behavior with known theoretical results and concepts must be demonstrated. Therefore, the first part of this thesis deals with obtaining and describing these results. Lastly, a depletion force is introduced to the self-propelled particles near the boundary and it's effect on the residence of particles near the boundary is examined.

Chapter 2

Model

2.1 Equations of motion

The equations of motion being used have been already briefly described in the introduction: properties of self-propelled motion. Here, a more detailed description is provided.

2.1.1 Brownian particles

To describe diffusion of Brownian particles, the following Langevin equations are numerically integrated:

$$\begin{aligned}\dot{x} &= \xi_{0,x}(t) \\ \dot{y} &= \xi_{0,y}(t)\end{aligned}\tag{2.1}$$

Where $\xi_0(t) = (\xi_{0,x}(t), \xi_{0,y}(t))$ is a 2D thermal Gaussian noise with correlation function $\langle \xi_0(t) \rangle = 0$, $\langle \xi_{0,i}(t) \xi_{0,j}(t) \rangle = 2D\delta_{ij}\delta(t)$, with $i,j=x,y$. D is the translational diffusion constant of a passive particle at a certain temperature [9],[39]. It is also important to mention, that at any time step the random generated number ξ needs to be integrated for a first order integration with the square root of the time step Δt . This is because we are dealing with a Wiener process which is the integral of the random noise: $\int_0^\tau \xi(t) dt$. We can view ξ as the steps of a random walk and $w(\tau)$ as the increments or the total distance covered at a time τ . Because of the diffusive nature of random walks, this distance scales as $\sqrt{\tau}$. All simulations are made using Matlab [40].

2.1.2 Self-propelled particles

To analyze active diffusion of self-propelled particles, the following Langevin equations are numerically integrated:

$$\begin{aligned}\dot{x} &= v_0 \cos(\theta) + \xi_{0,x}(t) \\ \dot{y} &= v_0 \sin(\theta) + \xi_{0,y}(t) \\ \dot{\theta} &= \xi_\theta(t)\end{aligned}\tag{2.2}$$

$\xi_0(t)$ is the same Gaussian noise as described in 2.1.1, the subsection above, ξ_θ is an independent 1D Gaussian noise with $\langle \xi_\theta(t) \rangle = 0$ and $\langle \xi_\theta(t) \xi_\theta(0) \rangle = 2D_{rot}\delta(t)$, which models the fluctuations of the propulsion angle θ . In this thesis the angle θ will be measured as the angle between the x-axis and the direction of self-propulsion.

2.2 Mean squared displacement

In this thesis, a quantity called the mean squared displacement (MSD) will often be used to characterize the diffusion of certain systems. Therefore it is worth it to go in a bit more detail about this statistical tool. The MSD is a measure for the deviation between the position of a particle and a reference position over time t , another way of interpreting the MSD is as a measure of the portion of the system explored. For a multidimensional space, Brownian motion must satisfy the following equation:

$$MSD(t) = 2dDt, \quad (2.3)$$

where d denotes the dimensionality of space and D the diffusion constant. This equation will only hold for isotropic and unrestricted translational diffusion and when the particles are spherical.

The MSD in this thesis is calculated as follows:

$$MSD(t) = \langle \Delta r^2(t) \rangle = \left\langle \frac{1}{N} \sum_{i=1}^N [\mathbf{r}_i(t_0 + t) - \mathbf{r}_i(t_0)]^2 \right\rangle_t, \quad (2.4)$$

where N is the number of particles and $\langle . \rangle_t$ represents averaging over initial times t_0 . For the systems in this thesis, time averaging and ensemble averaging are used. Generally 10 different initial times are used for time averaging, but sometimes this can be increased for systems where computation time increases non-linear with the amount of particles being simulated. For example when calculating a system where particles are interacting it can be useful to use decrease the amount of particles and increase initial time averaging. To illustrate this process, Figure 2.1 shows the results of the averaging procedure of 10 free Brownian particles. A blue curve is a time averaged MSD curve of one particle. The red curve is the average of all the (blue) time averaged curves. Figure 2.1 shows the averaging procedure for 10 particles and time averaging over 10 initial times, Figure 2.2 shows the same averaging, but for 1000 initial times. The effect is clear: much smoother curves are found in Figure 2.2. It must be noted that the MSD will be displayed in a log-log scale, this is a method for dealing with large values often created by this tool. The large values are a consequence of squaring a cumulation of displacements over time. A final argument for using this scale is to follow the example of literature on this topic in order to compare (most) results more easily.

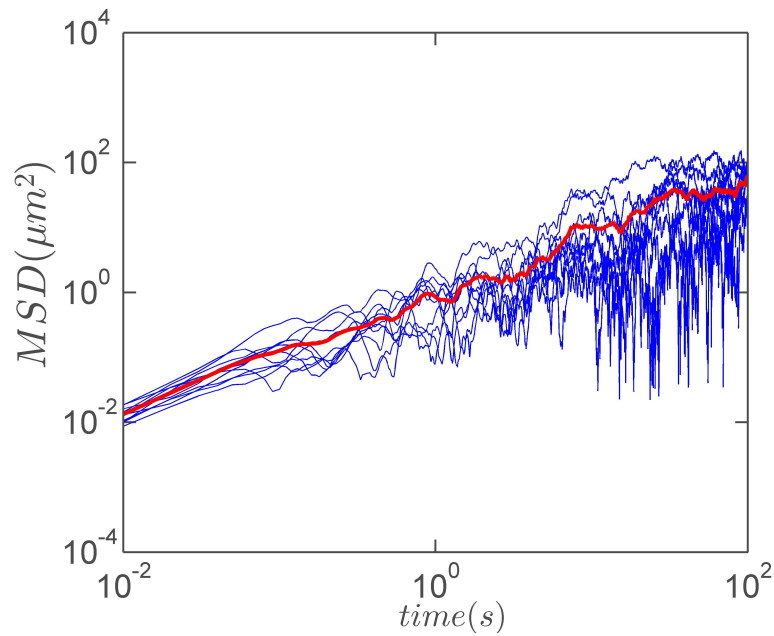


Figure 2.1: Illustration of the averaging procedure: the blue curves are time averaged curves, each corresponding to a trajectory of one Brownian particle. The red curve is the average of all the blue curves.

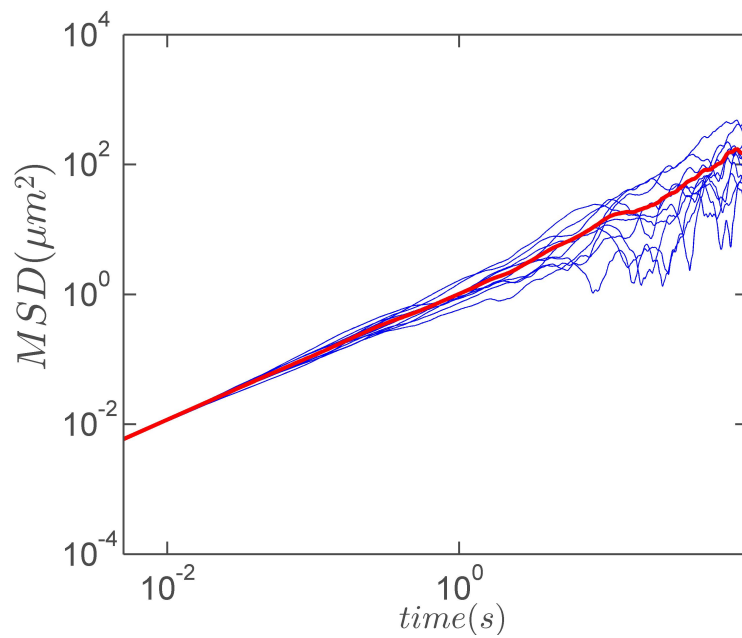


Figure 2.2: Same averaging procedure as in Figure 2.1 only now, the initial time averaging is increased to averaging over 1000 initial times. The results are much smoother curves. In cases where ensemble averaging is difficult, initial time averaging is increased.

Chapter 3

Results & Discussion: Brownian particles

In this chapter, various systems with free and interacting Brownian particles are studied. The first reason being to compare with known theory and therefore have confirmation of the code being able to adequately reproduce well-known systems, the second reason is to have an insight in what the contributions of Brownian motion might be of these systems when using active Brownian particles.

3.1 Free Brownian particles

Free Brownian particles are simulated using the over-damped Langevin equations described in the introduction and chapter 2, this is to check if the code can reproduce simple, well understood systems before going to more complex simulations. The diffusion constant of free Brownian particles is given by the following equation:

$$D = \frac{k_B T}{6\pi\eta R} \quad (3.1)$$

Where k_B is Boltzmann's constant, T the absolute temperature, η the viscosity of the medium and R the radius of the particles. Using equation (3.1), the MSD of experimental Brownian particles in Ref.[23] can be simulated. T is set equal to the room temperature: 295.15 K. The radii of the particles are on average $1,62 \mu m$, the viscosity of water is approximately $9 \times 10^{-4} Pa.s$ ($Pa = \frac{N}{m^2}$). An illustration of the simulated Brownian trajectories is shown in Figure 3.1 (a). The MSD of the simulated particle trajectories is displayed in Figure 3.1 (b). Theoretically the MSD is proportional to time: $MSD \propto t^\alpha$, $\alpha = 1$. Numerically, a good agreement is found: $\alpha = 1.0105$ (see legend Figure 3.1 (b)). At time $t=3s$, the value of the MSD is $3.67 \mu m^2 \pm 0.08 \mu m^2$, which is in good agreement with the experimental value in Figure 3.1 (c). This shows that the model being used is adequate for simulating Brownian motion.

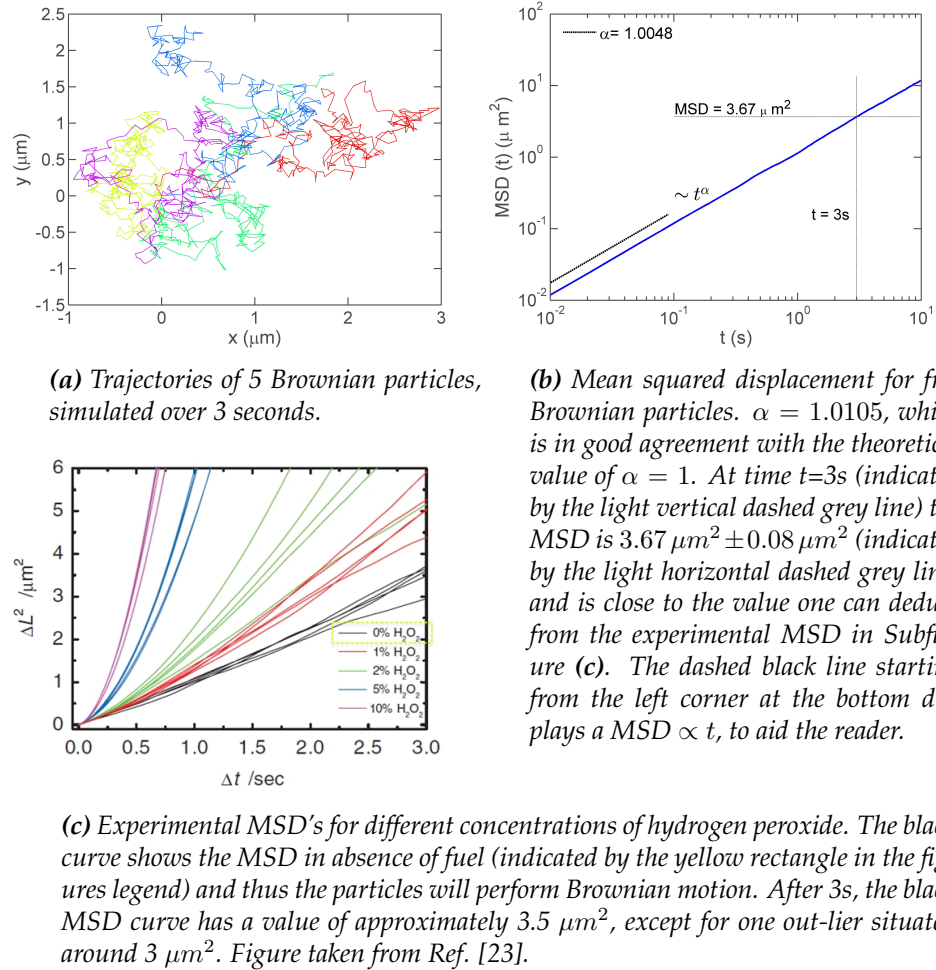


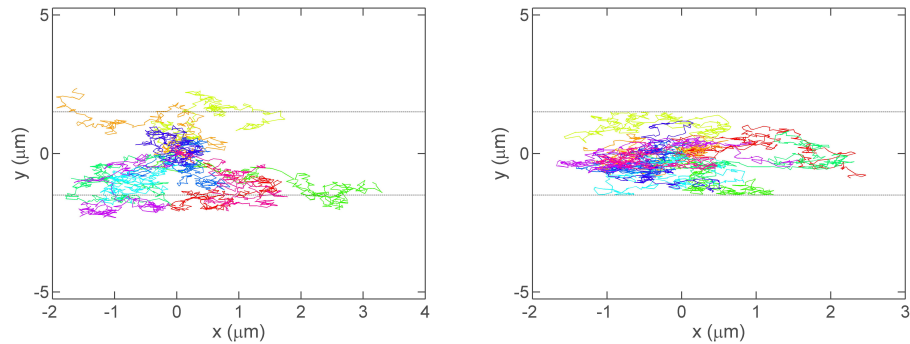
Figure 3.1

3.2 Reflecting boundary

Here, the effect of adding a reflecting boundary in a system of non-interacting Brownian particles is studied. The reflecting angle will be the same as the incident angle. In Figure 3.2 **(a)** trajectories of 10 free Brownian particles are simulated over 3s to show the spatial extent of those particles in this given time. In Figure 3.1 **(b)** and **(c)** the MSD evaluated at $t=3$ was approximately $3.67 \mu\text{m}^2$. Since particles have already a significant chance to encounter the boundary at time $t \approx 3s$, it is expected that the MSD evaluated at this time will be different since the particles become restricted in one spatial dimension, namely the y-direction. Theoretically it is known that the MSD for free Brownian particles in any dimension is proportional to t :

$$\langle |\mathbf{r}(t_0 + t) - \mathbf{r}(t)|^2 \rangle = 2dDt, \quad (3.2)$$

where d is the dimension of space, D the translational diffusion constant.



(a) Trajectories of 10 Free non-interacting Brownian particles, simulated over 3 seconds. This figure shows that almost all particles would have reached the boundary if the boundary was "activated". This indicates that a deviation of the value of the experimental and numerical MSD can be expected for $t=3s$.

(b) Trajectories of 10 non-interacting Brownian particles in a channel with boundaries at $\pm 2.31 \mu\text{m}$, simulated over 3 seconds.

Figure 3.2

In Figure 3.3, the MSD for early times and later times is approximately proportional to t^α , $\alpha \approx 1$, indicated by the black dotted lines close to the blue curve. These lines are fits for those short-and long times and the exponent of the fit is displayed in the legend. In between those two black dotted lines, there is a regime where a crossover occurs: particles are starting to encounter the boundary and this has an effect on the rate of diffusion and thus on the diffusion constant. Equation (3.2) shows that the diffusion constant for two dimensions is double the diffusion constant in one dimension. In figure 3.3, the diffusion constants for early times and longer times are shown in red and it is found that the diffusion constant for longer times ($0.15 \mu\text{m}^2\text{s}^{-1} \pm 0.02 \mu\text{m}^2\text{s}^{-1}$) is roughly half the constant for shorter times ($0.292 \mu\text{m}^2\text{s}^{-1} \pm 0.002 \mu\text{m}^2\text{s}^{-1}$). The MSD at $t=3s$ for reflecting boundaries is $2.41 \mu\text{m}^2 \pm 0.11 \mu\text{m}^2$ and indeed smaller than the MSD without boundaries: $\text{MSD} = 2.41 \mu\text{m}^2 \pm 0.11 \mu\text{m}^2$. A long simulation time (500 s) to calculate the MSD is used to make sure all the particles "experienced" the limitation in the y-direction in order to have a MSD curve that displays the two features of the system. First thermal Brownian motion, second restricted thermal Brownian motion.

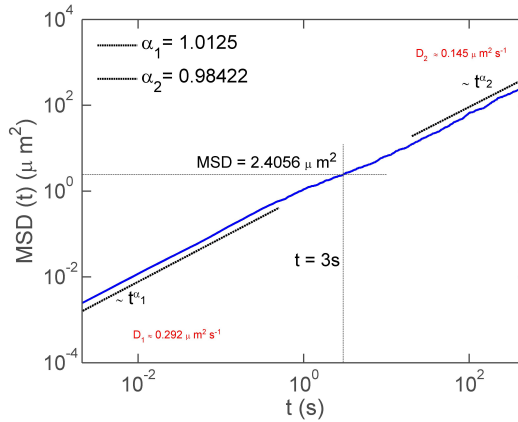
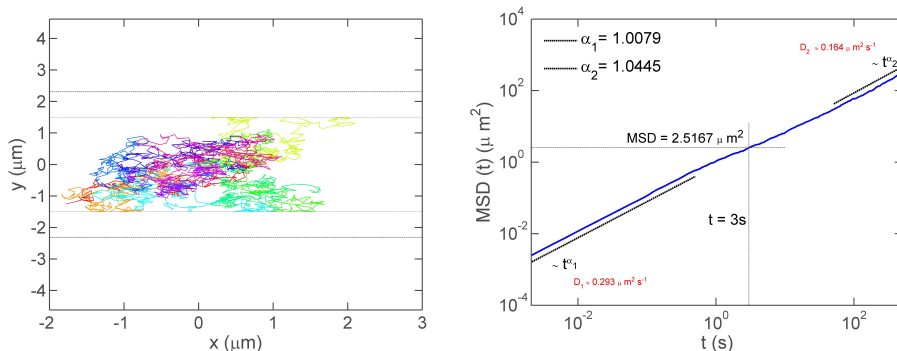


Figure 3.3: Simulated MSD over 500 seconds. At short and long times, the MSD is proportional to t^{α_1, α_2} with $\alpha_1, \alpha_2 \approx 1$. The diffusion constant D_1 for short times is $0.292 \mu\text{m}^2 \text{s}^{-1} \pm 0.002 \mu\text{m}^2 \text{s}^{-1}$ and for long times D_2 is found to be $0.145 \mu\text{m}^2 \pm 0.02 \mu\text{m}^2$. The MSD at $t=3\text{s}$, is equal to $2.41 \mu\text{m}^2 \pm 0.11 \mu\text{m}^2$ which is approximately the same value as for reflective boundaries.

3.3 Sliding boundary

Here, non-interacting Brownian particles encountering a frictionless sliding boundary are studied. When a particle encounters such a boundary, the particle will slide along this boundary until the random thermal noise kicks the particle away from the boundary. Results similar to the reflective boundaries are observed. The diffusion constant for short times is $0.293 \mu\text{m}^2 \text{s}^{-1} \pm 0.002 \mu\text{m}^2 \text{s}^{-1}$ and for long times we found $0.16 \mu\text{m}^2 \text{s}^{-1} \pm 0.02 \mu\text{m}^2 \text{s}^{-1}$. And the MSD at $t=3\text{s}$ is $2.52 \mu\text{m}^2 \pm 0.2 \mu\text{m}^2$.



(a) Trajectories of 10 non-interacting Brownian particles encountering a sliding boundary at $y = 2.31 \mu\text{m}^2$ simulated over 3 seconds.

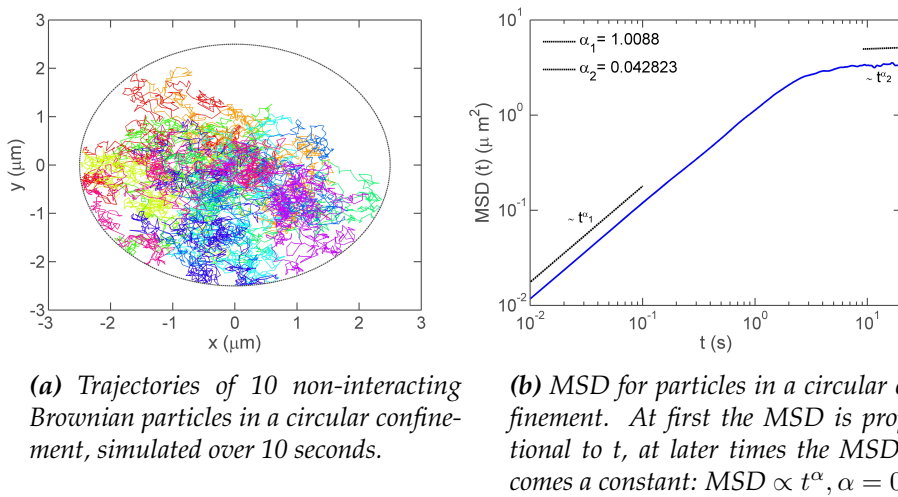
(b) Simulated MSD over 500 seconds. Similar behavior as depicted in Figure 3.2 (c) is found: short and long time proportionality of the MSD with t^{α_1, α_2} with $\alpha_1, \alpha_2 \approx 1$

Figure 3.4

Figures 3.3 & 3.5 suggest that the difference between reflective and sliding boundaries for Brownian particles is not very significant. Both have almost the same diffusion constants for short and long times. Also, there long term exponents are both approximately 1. When the MSD is evaluated at time=3s: there values are also approximately the same.

3.4 Circular confinement

A very simple system wherefore the MSD can be intuitively predicted is a circular confinement. At first, the particles are free to move but for longer times, the particles are confined in all directions and thus the MSD will saturate, i.e., become a constant. This confinement is illustrated in Figure 3.5 (a) and the MSD of this system is shown in Figure 3.5 (b).



(a) Trajectories of 10 non-interacting Brownian particles in a circular confinement, simulated over 10 seconds.

(b) MSD for particles in a circular confinement. At first the MSD is proportional to t , at later times the MSD becomes a constant: $MSD \propto t^\alpha$, $\alpha = 0$.

Figure 3.5

The boundaries of this circular confinement are reflective boundaries, Figure 3.5 (b) shows that the results are in line of expectations: a short time exponent $\alpha_1 \approx 1$ and a long time exponent $\alpha_2 \approx 0$.

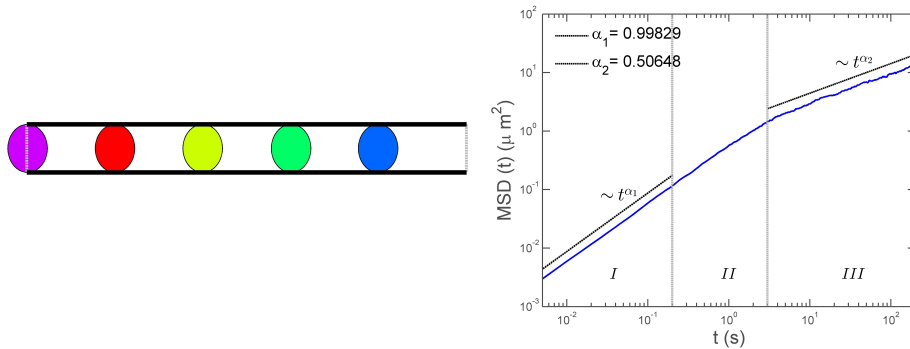
3.5 Single-file diffusion

Single-file diffusion is any type of diffusion where the particles are limited to one dimension and cannot leap over each other. The concept of SFD was introduced decades ago in bio-physics [41], to account for the transport of water and ions through molecular-sized channels in membranes, and it was developed in early theoretical works [42] [43] [44]. Particles in a single file can interact with each other via different inter-particles interactions, e.g. hard-core interaction, soft-core interaction, Yukawa interaction. In this thesis a soft-core repulsive interaction is used for the interaction between these particles. Further interactions in this thesis will also be soft-core interaction. The repulsive force in the soft-core model can be described as:

$$\mathbf{F}_{i,j} = k(2r_0 - r_{i,j}) \text{ if } r_{i,j} < 2r_0 \quad (3.3)$$

Where k is a scaling factor, r_0 is the radius of the particles and $r_{i,j}$ is the distance between the center of two particles. This way $2r_0 - r_{i,j}$ corresponds with the overlap between two particles.

Periodic boundary conditions are used to ensure a constant particle density. Figure 3.6 (a) illustrates schematically the system being simulated, i.e. spherical particles only allowed to move in one direction. As soon as the center of a particle crosses the light gray line at the end of the file, it will jump to the other side if the repulsive force it would experience on the other side is not too great to push it back. Because of this "jumping", it is important to make corrections to the displacements of the particles. Otherwise the MSD will display sudden jumps. Figure 3.6 (b) shows the MSD of this system. Three regimes can be defined, indicated by the Roman symbols: *I*, *II* and *III*. In Regime *I*, particles behave like free Brownian particles since they do not interact with each other. As time continues, the particles diffuse and will start to interact with each other and the diffusion becomes more restricted, this is Regime *II*. In the last Regime, all particles are feeling the restrictions in diffusion. Theoretically it is known that the single-file MSD curve for long times is proportional to t^α , $\alpha = 0.5$. A good agreement is found with previous theoretical works (see, e.g., [45]): $\alpha = 0.51 \pm 0.03$, see the legend of Figure 3.6 (b).



(a) 5 interacting Brownian particles in a channel that only allows displacements in the x -direction. Periodic boundary conditions are used to keep the particle density constant.

(b) MSD of single file diffusion. In regime *I*, the particles display normal Brownian behavior, i.e. $MSD \propto t^\alpha$, $\alpha = 1$. Regime *II* is a crossover regime from *I* to *III*. Here, particles start to interact with each other. Regime *III* is characterized by $MSD \propto t^\alpha$, $\alpha = 0.5$.

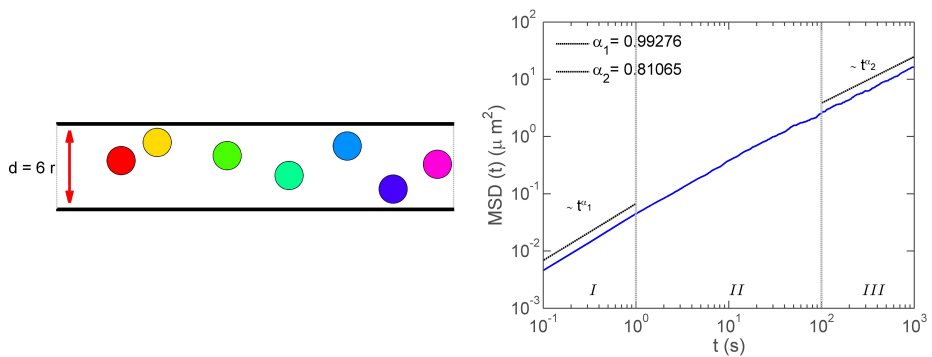
Figure 3.6

3.6 Narrow channel

Since two limit cases have been studied: single-file diffusion and free Brownian diffusion, a narrow channel can be studied as a system in between these two cases. In a narrow channel, particles may leap over each other although this leaping is made more difficult due to a small channel width. In such a system one may expect a MSD that is proportional to t^α , $0.5 < \alpha < 1$ for long times. For this simulation the same repulsive force is used as described by equation (3.3).

3.6.1 Reflecting boundary

Only a narrow channel with reflecting boundaries is studied. Figure 3.7 (a) shows schematically a typical system that is simulated: a channel with a width that is a factor $d \times$ the radius r of the particles. The solid black lines represent the reflective boundaries while the grey lines represent the periodic boundary of the channel. Although there are only 7 particles shown in the figure, for the actual simulation 30 particles are used and each simulation is repeated 30 times. The reason being that a simulations with 30×30 particles is to taxing on computational time: each particle has to check if each other particle is within range for equation (3.3) to become active. Figure 3.7 (b) shows the MSD for a channel width $d = 6r$. The MSD for long times, regime III, shows a t^α , $0.5 < \alpha = 0.81065$ proportionality. Figure 3.8 shows α_2 , the exponent for long times, in function of the width of the channel. When the width becomes smaller than 2 times the diameter of the particles, e.g. $d = 3r$, particles cannot pass each other and $\alpha_2 \rightarrow \alpha_{SF}$, with $\alpha_{SF} (= 0.5)$ the long time exponent for single-file diffusion. As the width of the channel increases, α_2 goes towards the free limit exponent: ($\alpha_{free} = 1$). These results qualitative agree with the previous numerical studies [46].



(a) 7 Interacting Brownian particles in a narrow channel with a width d that is 6 times the radius r of the particles.

(b) MSD for interacting Brownian particles in a narrow channel of width 6 times the radius of the particles.

Figure 3.7

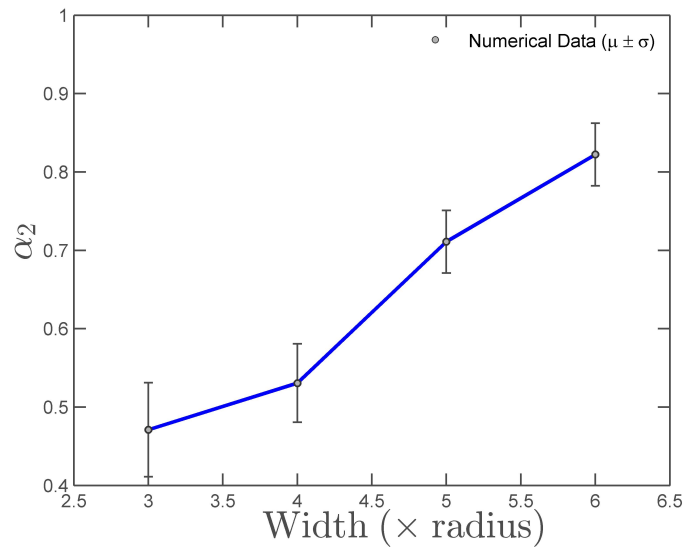


Figure 3.8: Long time exponent α_2 as a function of the channel's width. As the width increases, α_2 increases towards 1. These results qualitative agree with the previous numerical studies.

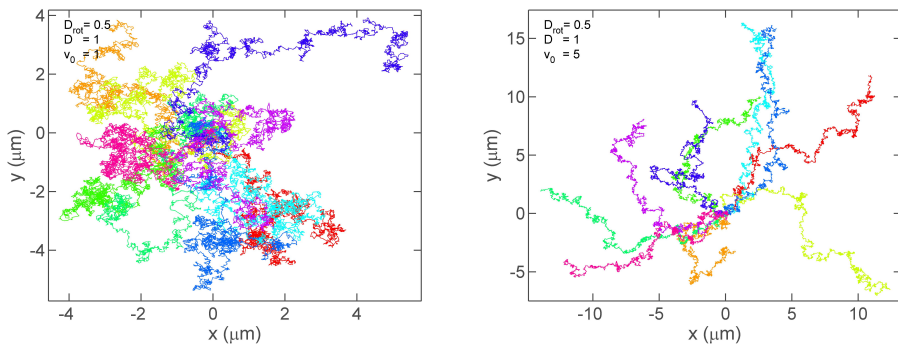
Chapter 4

Results & Discussion: self-propelled particles

In this chapter, the motion of active Brownian particles will be studied in various systems. From now on, the units for the rotational D_{rot} and translational diffusion D constants will be expressed in $\mu\text{m}^2 \text{s}^{-1}$, the self-propelled velocity v_0 is expressed in $\mu\text{m s}^{-1}$, dimensions will be expressed in μm .

4.1 Free active particles

Figure 4.1, Figure 4.2 and Figure 4.3 display the trajectories of 10 free non-interacting active particles starting in the origin. In Figure 4.1 (a) the trajectories resemble much the trajectories of thermal Brownian motion, only a small contribution from the self-propelled component can be distinguished, for example, the purple trajectory in the top right corner of seems to display motion along a certain direction. In Figure 4.1 (b), the strength of the self-propelled velocity v_0 is increased from 1 to 5. The self-propelled component becomes much more pronounced since the fraction of the contribution from Brownian motion is decreased. The Brownian component is still clearly present in the particles trajectories.

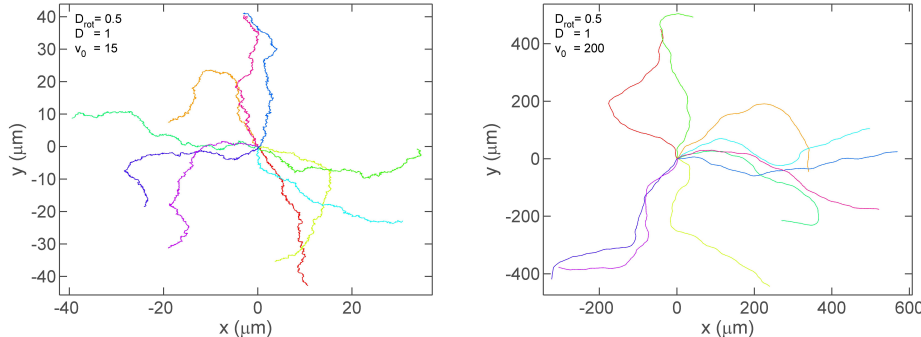


(a) 10 trajectories of free active Brownian particles starting from the origin. Here, the rotational diffusion constant $D_{rot} = 0.5$, the Brownian diffusion constant $D = 1$, and the strength of the self-propelled velocity $v_0 = 1$.

(b) Same parameters as in this Figure (a), except for the strength of the self-propelled velocity: $v_0 = 5$.

Figure 4.1

Increasing v_0 to 15 (see Figure 4.2 (a)) and to $v_0 = 200$ (see Figure 4.2 (b)) leads to trajectories where the thermal component is hardly noticeable and a great increase of the maximum displacement of the particles. For a self-propelled velocity of $v_0 = 200$, the curves are almost perfectly smooth.

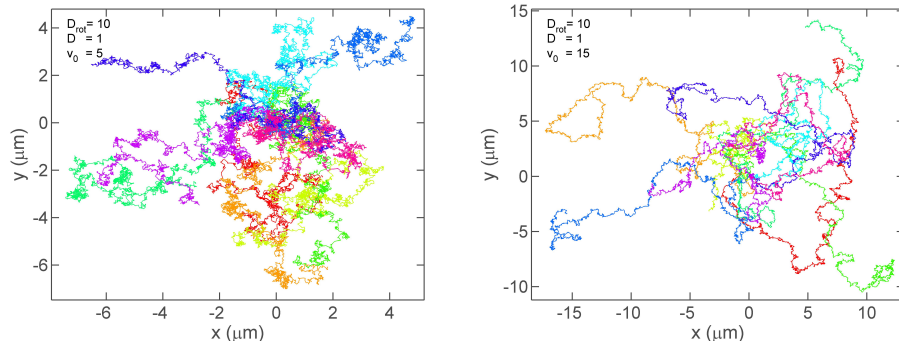


(a) 10 trajectories of free active Brownian particles starting from the origin. Here the rotational diffusion constant $D_{rot} = 0.5$, the Brownian diffusion constant $D = 1$, and the strength of the self-propelled velocity $v_0 = 1$. For $v_0 = 1$, it is difficult to distinguish the motion from thermal Brownian motion.

(b) Same parameters as in this Figure (a), except for the strength of the self-propelled velocity: $v_0 = 5$. The self-propelled component is clearly present in the trajectories. The maximum extent of the trajectories is also increased.

Figure 4.2

In Figure 4.3, the rotational diffusion constant D_{rot} is increased to 10 for particles with a self-propelled velocity of 5 (Figure 4.3 (a)) and $v_0 = 15$ (Figure 4.3 (b)). This increase of D_{rot} causes for both self-propelled velocities a much faster rotational diffusion and the trajectories already start to resemble thermal Brownian motion. The maximal spatial extent of the trajectories is also vastly decreased: notice the difference between Figure 4.1 (b) and Figure 4.3 (a) or between Figure 4.2 (a) and Figure 4.3 (b).



(a) 10 trajectories of free active Brownian particles starting from the origin. Compared with Figure 4.1 (b), the rotational diffusion constant is increased from 0.5 to 10, resulting in trajectories that resemble more thermal Brownian motion.

(b) Same parameters as in this Figure (a), except for the self-propelled velocity: $v_0 = 15$. Compared with Figure 4.2 (a), the spatial extent is vastly reduced.

Figure 4.3

The MSD for active particles, according to the theory, is proportional to $t^{\alpha_1}, \alpha_1 = 2$ for short times and proportional to $t^{\alpha_2}, \alpha_2 = 1$ for long times. Figure 4.4 shows the MSD curve for free active Brownian particles. For this simulation the diffusion constant $D = 1$, the rotational diffusion constant $D_{rot} = 0.08$ and the self-propelled velocity $v_0 = 200$. A Good agreement with theory is found for the short and long time exponents: $\alpha_1 = 1.997 \pm 0.005$ and $\alpha_2 = 1 \pm 0.04$. The parameters are chosen in such a way it is easy to display the ballistic feature at early times and the random motion at long times. If the rotational diffusion constant was taken to high, a faster deviation from the ballistic regime would occur and one would have to zoom in at smaller times to find the $t^{\alpha_2}, \alpha_2 = 2$ proportionality of the MSD. If v_0 is chosen to be smaller, another issue occurs: the Brownian noise contribution will decrease the short time exponent α_1 such that $1 < \alpha_1 < 2$.

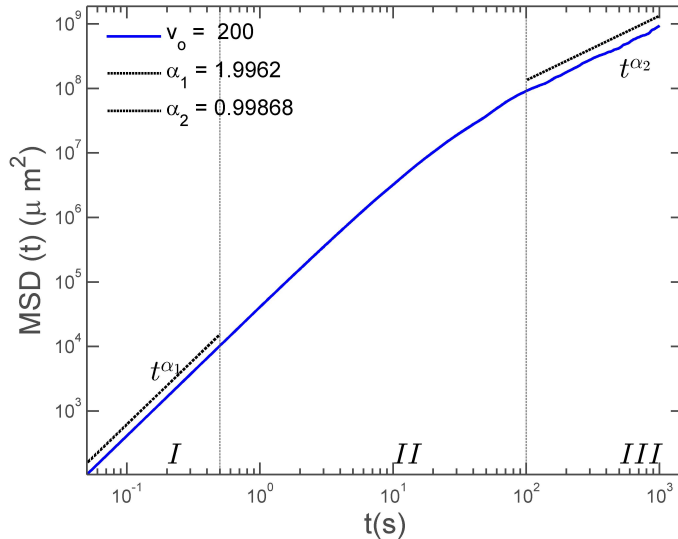


Figure 4.4: Mean squared displacement for free active Brownian particles. At early times (regime I) the proportionality is $t^{\alpha_1}, \alpha_1 \approx 2$, at longer times (regime III) the proportionality is $t^{\alpha_2}, \alpha_2 \approx 1$. $v_0 = 200$, Parameters: $D_{rot} = 0.08, D = 1$.

Figure 4.5 shows the MSD curves for different values of the self-propelled velocity ranging from 0.1 to 1000. From this figure, one can see that increasing v_0 from a certain value will lead to the same shape of curves shifted in the positive y-direction (black, cyan and yellow curve). When v_0 becomes smaller, a more complex shape is observed: the red and blue line in Figure 4.5. The Roman numbers *I*, *II* and *III* are used to label different regimes for high values of v_0 . *I* denotes the initial ballistic regime where the MSD is proportional to t^{α_1} , $\alpha_1 \approx 2$. *II* denotes an intermediary regime and *III* is the long time regime where $\text{MSD} \propto t^{\alpha_2}$, $\alpha_2 = 1$. The intervals of these regimes are constant for all v_0 starting from a threshold value (yellow line in this Figure). When the self-propelled velocity becomes smaller, e.g. $v_0 = 0.1$, the MSD is indistinguishable from a thermal Brownian MSD. This is shown by the green curve in Figure 4.5: the theoretical curve for Brownian diffusion ($\text{MSD}=2dt$) is plotted over this line (grey dotted line over the bottom green curve).

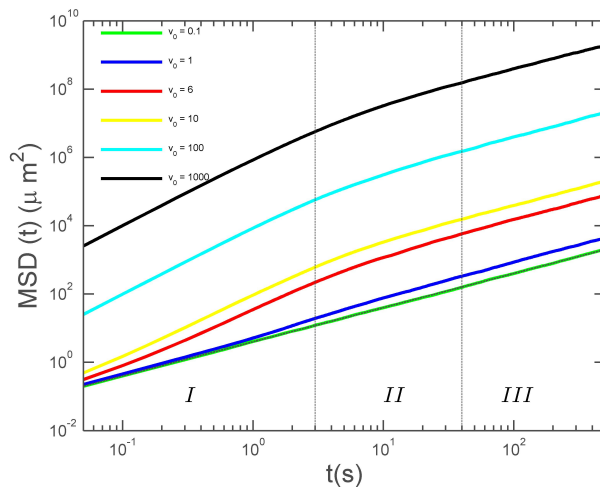


Figure 4.5: MSD curves for different values of the strength of the self-propelling velocity v_0 are shown. For each curve the rotational and Brownian diffusion constants are the same: $D_{\text{rot}} = 0.5$, $D = 1$.

For more intermediary values of v_0 , e.g. $v_0 = 1$, $v_0 = 6$ (blue and red curve in Figure 4.5), a more complex shape is found.

To observe this complex shape in more detail, Figure 4.6 shows only the red line from Figure 4.5. The maximum slope is not realized in the beginning of the curve, but rather somewhere in the middle (region *II*). Note that the regions in this figure correspond to the extent of the horizontal dimension (in this case time) where a fit is made (grey dotted line). In region *II*, the MSD is proportional to t^{α_2} , $\alpha_2 \approx 1.71$ while in region *I* the MSD is proportional to t^{α_1} , $\alpha_1 \approx 1.4$. For longer times the "normal" proportionality is again found to be $\text{MSD} \propto t^{\alpha_3}$, $\alpha_3 \approx 1$. This curious behavior is explained next.

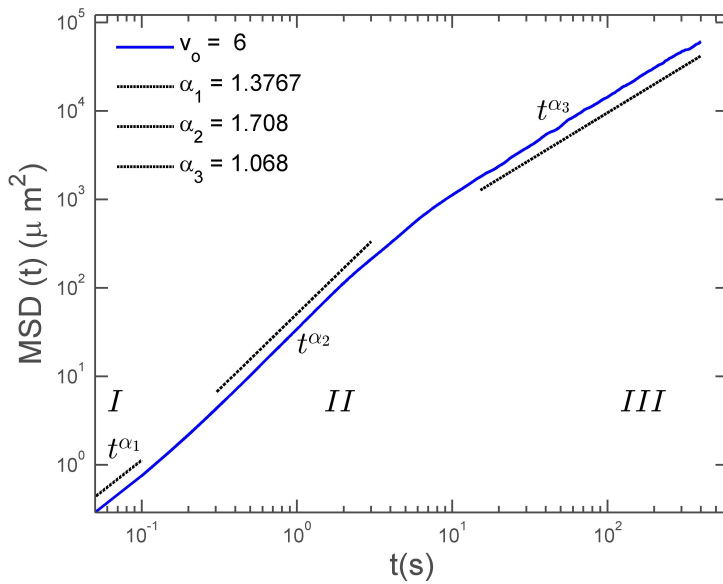


Figure 4.6: Close up of the red MSD of Figure 4.5. The MSD's slope is highest in region II rather than in region I.

When the self-propelled velocity becomes smaller, it will for a given time t , depending on the rotational diffusion constant, give a consistent push along a general direction. However when this push is smaller than the contribution delivered by the thermal Brownian noise, it does initially not show up in the MSD. Over time the effect becomes more noticeable and this will show up in the MSD as a rise. Of course this consistent push will not persist indefinitely and will display itself a Brownian motion for longer times. A schematic depiction of this process is provided by Figure 4.7.

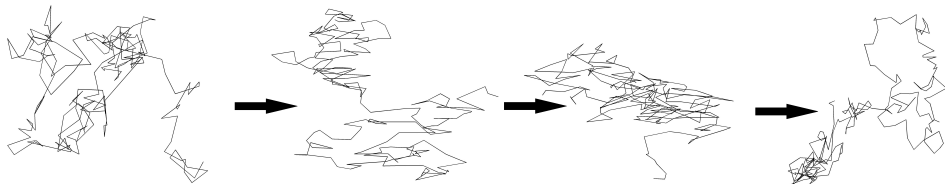
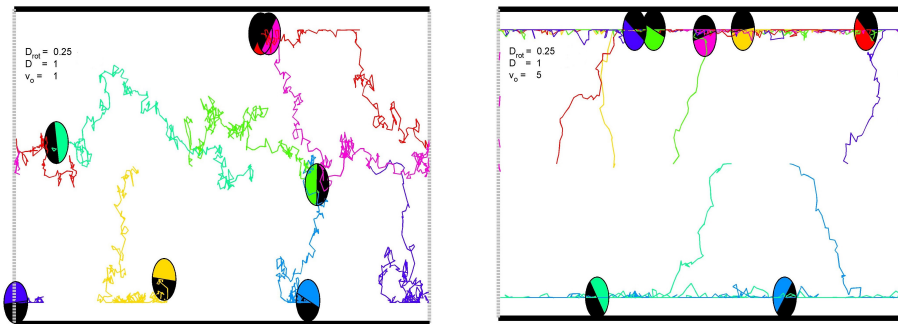


Figure 4.7: Schematic of the effect of a small self-propelled velocity. The thermal Brownian noise overrules the self-propelled component, but this component will, given a D_{rot} that is not too large, add up to movement in a certain direction. This can only be noticed at later times. The arrow indicates the consistent push along a fixed direction. Of course this schematic is a simplification: in a real system the trajectories will also be smeared out along this direction.

4.2 Sliding boundary

In this subsection, the effect of adding sliding boundaries to free active particles will be examined. An illustration of the typical system that is being simulated can be found in Figure 4.8. In this figure, one can already see what the effect of increasing v_0 might have on the residence of the particles at the boundary. In Figure 4.8 (a) v_0 is set 1 and the trajectories have a large amount of Brownian noise. There are four particles at the boundaries, and a significant part of their trajectories are away from the boundaries. In 4.8 (b) all the particles are near the boundaries and a greater part of their trajectories seem to be also near the boundaries. Clearly, the initial orientation of the particles plays a role: particles with the center of their black cap orienting more towards the normal of the boundary will reach this boundary faster, given that $\tau_{rot} \ll \tau_{width}$, where τ_{width} the average time for a particle to reach the boundary and τ_{width} the rotational diffusion time. This needs to be studied further using better statistics, but it will later be revealed that this is indeed the case.



(a) Trajectories of 7 Active non-interacting Brownian particles in a wide channel (width= $15 \times r$) with sliding boundaries (solid black lines) and periodic boundaries at the sides (dashed grey lines), simulated over 3 s. The middle of the black cap indicates the self-propelling direction.

(b) The same system as in (this) Figure (a) is simulated, except now the strength of the self-propelling velocity v_0 is increased from 1 to 5.

Figure 4.8

To illustrate the effect of changing the rotational diffusion constant, two supplementary videos are provided in Ref. [47] & Ref. [48]. Both videos show active Brownian particles in a wide channel (width= $15 \times r$). The first reference illustrates that particles with a low rotational diffusion constant will reside almost all of there time at the boundary. At some point in time even a mini-cluster that displayed a sort of collective movement was formed along the boundary. For a higher rotational diffusion constant the particles trajectories were much more homogeneous distributed in the channel. For this simulation the parameters were chosen in such a way that these characteristics are shown for short times, this explains the relative extreme values of some variables (shown in the video). Also, for real simulations, smaller time steps where used.

Figure 4.9 shows the MSD for active Brownian particles in channels with different boundary conditions. Sliding and reflective boundary conditions display a faster crossover to a regime where the MSD is proportional to t^α , $\alpha = 1$ and the diffusion constant of this regime is lower than that of free active particles. A small difference between sliding and reflecting boundary conditions is observed. This could be explained that for active particles, a sliding boundary will convert motion towards to boundary in motion along the boundary while reflecting boundaries will convert this motion to motion away from the boundary, but often the self-propelled component will still be directed towards the boundary, making this diffusion process somewhat more inefficient.

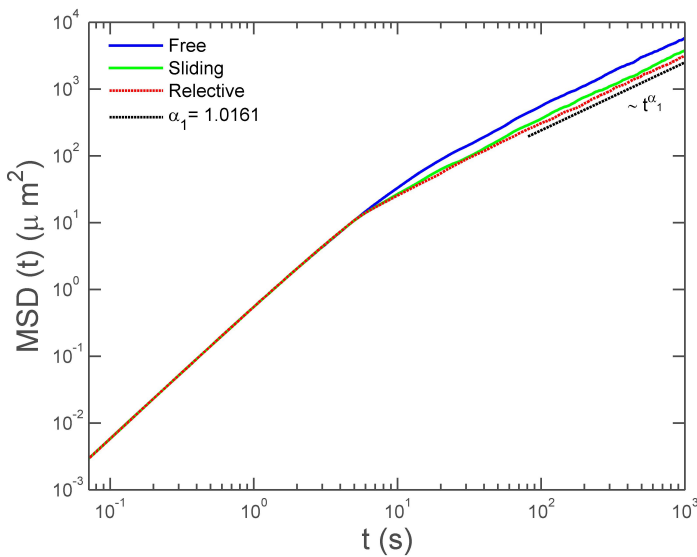


Figure 4.9: Effect of a sliding & reflective boundary on the MSD. The green curve & and the red curve show a faster crossover to the regime where $MSD \propto t^{\alpha_2}, \alpha = 1$. The sliding boundary displays a crossover to a diffusion constant lower than for free active particles and a reflective boundary crosses over to a slightly lower diffusion constant than for a sliding boundary.

4.3 Narrow channel

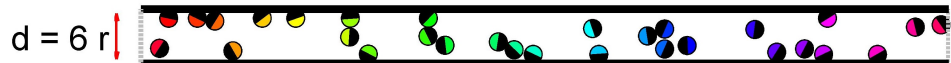
In this section, the behavior of active Brownian particles will be studied in a narrow channel for sliding and reflecting boundary conditions.

4.3.1 Sliding boundary

First, 30 active particles are simulated over 100 s for sliding boundary conditions in a narrow channel with a width d that is 6 times the radius r of the particles (not that this corresponds to the size of the narrow channels in the experiments of Ref. [9]). Figure 4.10 shows the distribution of particles over different time intervals. 4.10 (a) At time 0 s, the particles are placed at an equal distance from each other, with randomized initial orientations at a constant height $h = \frac{1}{2}d$. 4.10 (b) At time 0.1 s most particles have reached the boundary and the particles are roughly in the same order they were placed in. This can be noticed by observing the subsequent colors in the channel. 4.10 (c) At time 100 s, the initial order can not be detected anymore. Most particles are at the boundary and the particles are more clustered than before. For all the simulations the following parameters were used: $D = 1$, $v_0 = 5$ and $D_{rot} = 0.5$.



(a) Time=0 s. Initial positions of 30 Interacting self-propelled particles in a narrow channel with width $d = 6r$.



(b) Time=0.1 s. Most particles have reached the boundary and the particles are still roughly in the same order as the order they were placed in.



(c) Time=100 s. Almost all particles are near the boundary except for two particles that are trapped somewhere in the middle. They are also more clustered than before.

Figure 4.10

Figure 4.11 shows that the clustering at large time is independent of the initial positions of the particles. Whereas the particles in Figure 4.10 were placed in a row, in Figure 4.11 (a) they are placed in a random fashion, without overlapping. However, at smaller times, a difference may play out because the particles are hindering each other more in reaching the boundary when they are placed randomly. This can be seen in Figure 4.11 (b), here a significant smaller portion of particles have reached the boundary than was the case in Figure 4.10 (b). Figure 4.11 (c) shows the same type of configuration for larger times as Figure 4.10 (c), namely: most particles have reached the boundary whilst the particles are more clustered.

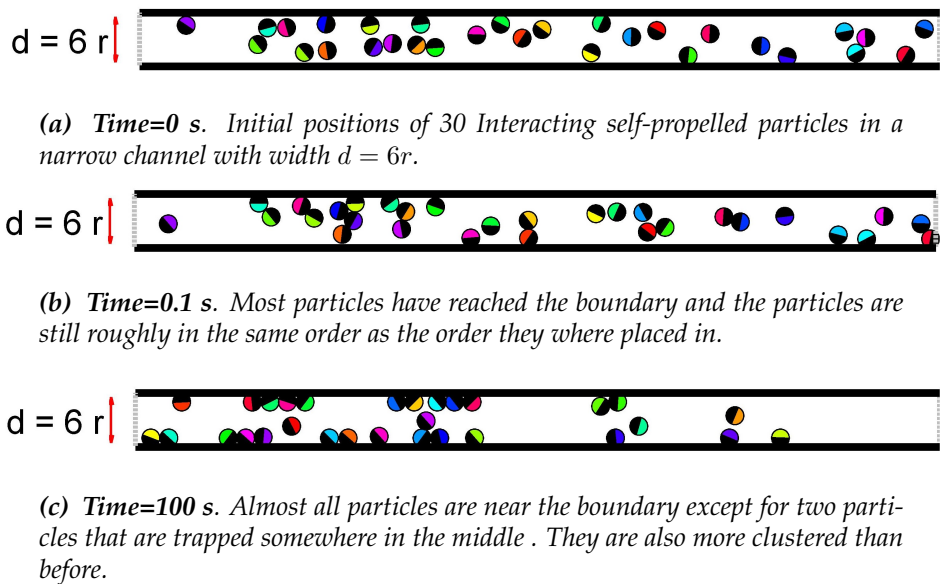


Figure 4.11

Figure 4.12 shows different time intervals for the same system described above, but for a higher particle density. 4.12 (c) The clustering of particles is more pronounced for this particle density: more particles are getting trapped in the middle of the channel, see the red box of Figure 4.12. Note that the concentration of the particles near the boundaries of the channel and clustering of the particles such that they clog the channel (see Figure 4.12 (c))) resemble the behavior observed in the experiment [9] where the clusters are formed by a mixture of passive and active particles (see Figures 1.17 and 1.18).

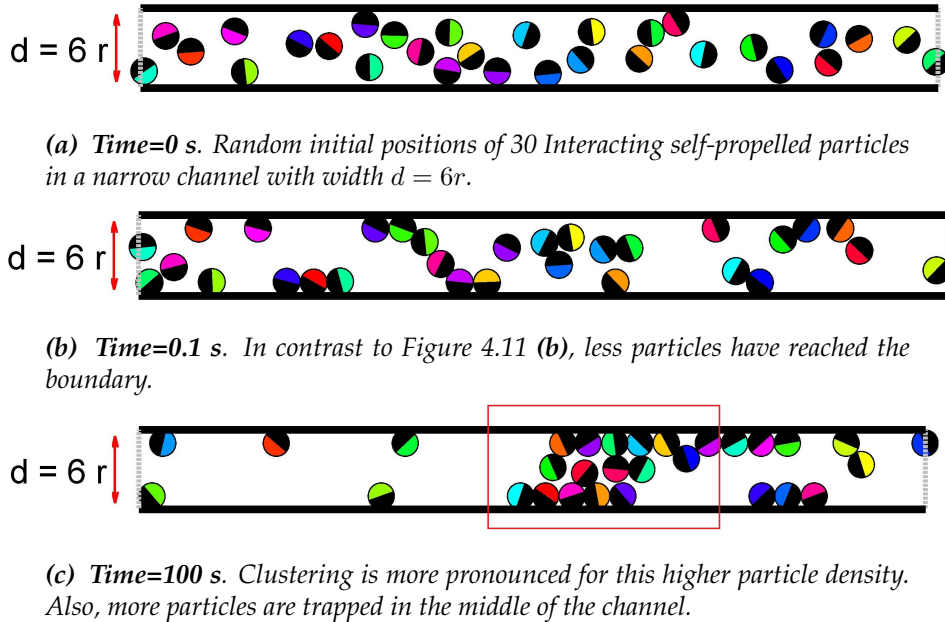


Figure 4.12

4.3.2 Reflective boundary

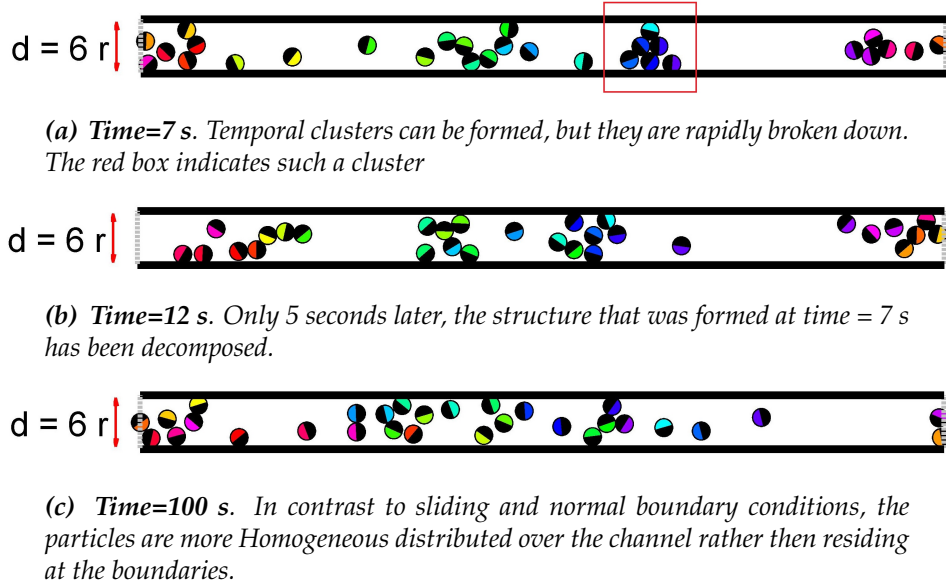
The difference between reflective and sliding boundary conditions on the positions of the particles is not directly apparent. When the orientation of the particles is preserved, the particle will after being reflected, return towards the boundary. Figure 4.13 is very similar to Figure 4.11 (c)



Figure 4.13: Time=100 s. No apparent difference can be observed between sliding and reflecting boundary conditions.

4.3.3 Random boundary

Reflecting boundary conditions that preserve the particles orientation did not result in an apparent difference of the particles positions with respect to the boundary. Here, a random boundary will reflect an incoming particle while simultaneously randomize the particles orientation. It was observed that clustering can still happen, however this clustering is unstable because of the random boundary conditions. Figure 4.14 (a) shows an example of such a temporary cluster. 5 Seconds later, the cluster is almost completely deconstructed in Figure 4.14 (b). 4.14 (c) Time = 100 s, particles are more homogeneous distributed across the channel when using reflective or sliding boundary conditions.

*Figure 4.14*

Lastly Ref. [49] can be mentioned. This study reports that for sufficiently strong self-propulsion of spherical microswimmers, phase separation into a dense cluster coexisting with a low-density disordered surrounding occurs. This is also what is observed in our numerical simulations presented in this section for sliding and reflecting boundary conditions, especially when using a higher particle density.

4.4 Trapping time

In this section, the relative attachment, or trapping, time of self-propelled particles near boundaries (i.e., the ratio of the time of a continuous residence of a particle near the boundary to the total observation time) will be studied as a function of the rotational diffusion constant, self-propelled velocity and the Brownian diffusion constant. The algorithm to calculate the trapping time considers a particle being trapped by the boundary when it's surface touches the boundary. When the distance between the boundary and the particle is within the range of 1.5 times it's radius, it will be considered attached when it returns to the boundary within three time steps. A particle will be considered detached anytime when the particle crosses this threshold or when the particle is not in direct contact with the boundary for more than three time steps. To further clarify this process, a schematic overview is given in Figure 4.15. The particles trajectory starts on the left of the figure, note that each element of the trajectory is labeled starting from 1. At time step 2, the particle moves towards the boundary located at $y=1$. The algorithm starts to count when the particle hits the boundary at time step 3. At the 5th time step, the particle is detached but the distance from the center of the particle to the boundary is smaller than the threshold distance $R_{thresh} = 3r = 0.075$ and the particle will still be considered trapped. The same applies for the 6th and 7th time step: the distance is smaller than the threshold and the particle doesn't detach longer than three time steps in succession from the boundary. At time step 8, the particle is again in contact with the boundary and it may detach again for 3 consecutive time steps within the distance R_{thresh} . The particle exceeds R_{thresh} at time step 9 and will be considered detached. Figure 4.16 illustrates that the 8th time step exceeds the threshold of detachment from the boundary and thus the trapping time will be the same as in Figure 4.15. This process can also be visualized by drawing an area around the boundary with a width of 2 times the radius. Once the particle is completely outside this area, it is no longer considered attached. When it is not touching the boundary for longer than 3 time steps, the 4th time step will also not be considered attached even though it is still inside this area. The area is shown in Figures 4.15 and 4.16 by the blue rectangle.

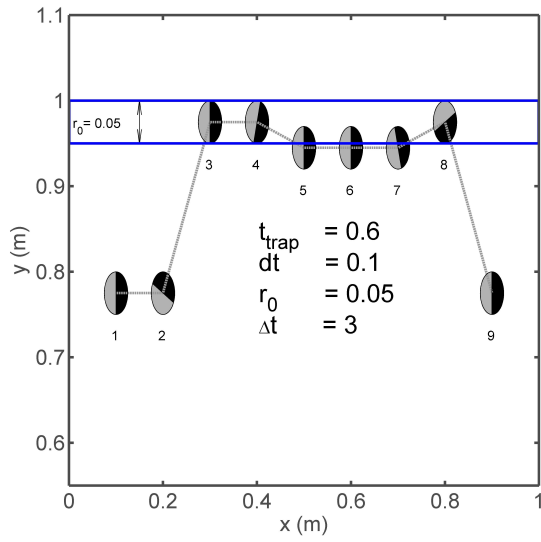


Figure 4.15: Illustration of the algorithm being used to calculate the attachment/trapping time. The particle is considered attached at time steps 3,4,5,6,7 and 8. In the middle of the figure various values are given. t_{trap} : the resulting trapping time in seconds, dt : the time interval between each displayed position, r_0 : the limiting distance, Δt : the maximum amount of time steps a particle may detach within the specified distance r_0 .

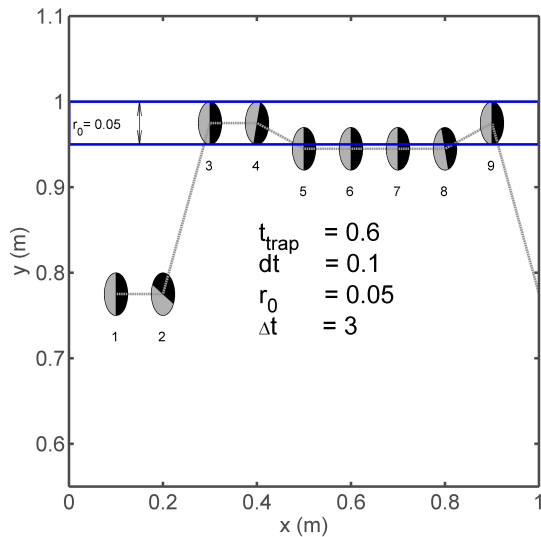


Figure 4.16: Illustration of the algorithm being used to calculate the attachment/trapping time. The particle is considered attached at time steps 3,4,5,6,7 and 9.

4.4.1 Trapping time versus the self-propelled velocity

When increasing the self-propelled velocity of a particle, the average trapping time at the boundary will increase, in general, very fast. This is because to avoid collision with a boundary, the orientation of the self-propelling component has to be closer and closer parallel to the x-axis for increasing v_0 , because the rotational diffusion time is too small to keep the particles from reaching the boundary in the simulated time. For a given D_{rot} , we can see in Figure 4.17 that the Brownian diffusion constant will only be able to play a role in the trapping of a particle when a certain threshold value is reached: the blue ($D = 0.001$) and green curve ($D = 1$) almost overlap perfectly. For $D = 100$ (red curve), the effect is more clear. For a very low v_0 the average trapping time will increase when D is increased. This is because when v_0 is very low, one can think of this system as a system that approaches normal Brownian motion. For those systems it is obvious that increasing D results in a higher trapping time: the particles reach the boundary more frequently because of a higher rate of diffusion; of course, they will not stay there for very long time, but the time it takes to again reach a boundary is lower as D increases. When v_0 starts to become a significant factor, increasing D will lower the trapping time because it has a chance to repel the particle from the boundary when the self-propelled velocity is still directed towards the boundary where the particle is trapped. This effect is best illustrated in the black curve of Figure 4.17: here one can clearly see the trapping time for small v_0 is higher than for the other curves, while for higher v_0 the trapping time decreases. When D is even further increased to $D = 10^4$, the trapping time becomes independent of v_0 (grey dotted line in Figure 4.17).

The results of this analysis provide important information on the trapping time of self-propelled particles that can be of interest for experiments with self-propelled particles in narrow channels. One important conclusion is that, for a wide range of the diffusion constants typical for experiments, i.e., ranging from $D = 0.001$ to 10 , even moderate values of the self-propelled velocity, $v_0 \approx 2 \mu\text{m s}^{-1}$, provide relatively high values of the trapping time, $t_{trap} > 0.7$. Also, it is worth noticing that the $t_{trap}(v_0)$ -curve shows a saturation for the values of the diffusion constant lower than $D = 10$, i.e., the value of $D = 10$ is a sufficient lower bound that provides a fast increase of t_{trap} with increasing v_0 .

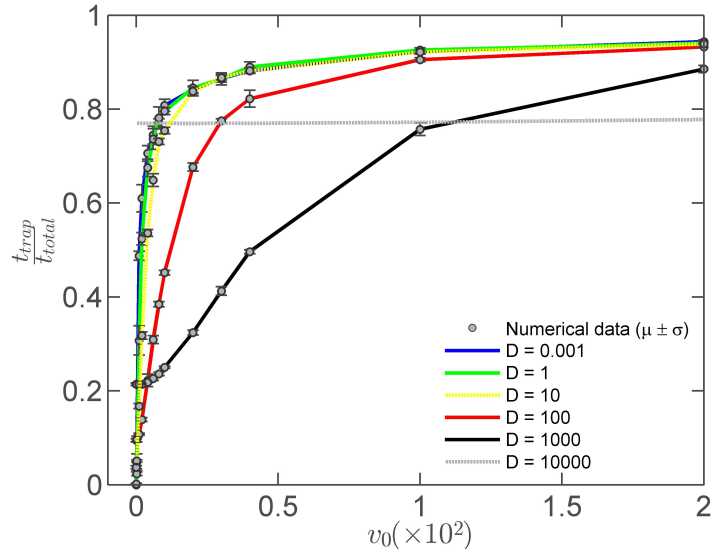


Figure 4.17: Relative trapping time as a function of the strength of the self-propelled velocity v_0 for a system with a width of 20 and a rotational diffusion constant $D_{rot}=0.5$. The different curves correspond to different Brownian diffusion constants. Simulation time = 25 s.

In Figure 4.18 the effect of different D_{rot} is showed. A similar effect as in Figure 4.17 occurs. The larger D_{rot} , the lower the average trapping time. The difference with Figure 4.17 is that even for lower v_0 the relative trapping time becomes also smaller as D_{rot} is increased. When a particle reaches the boundary it will of course detach faster as D_{rot} increases, the larger D_{rot} , the more it will cancel the effect of increasing v_0 .

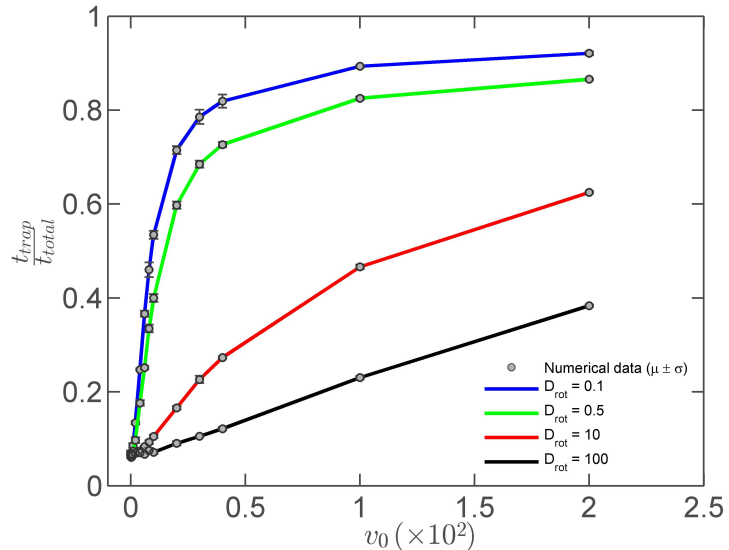


Figure 4.18: Relative trapping time at the boundaries as a function of the strength of the self-propelling velocity for different values of the rotational diffusion constant D_{rot} . The higher D_{rot} , the smaller the relative trapping time. $D = 5$, channel's width = 20, simulation time = 25 s.

When increasing the width of the channel, clearly the relative trapping time decreases. For a very large width (width=2000, see black curve in Figure 4.19) and low v_0 , the particles do not even reach the boundary.

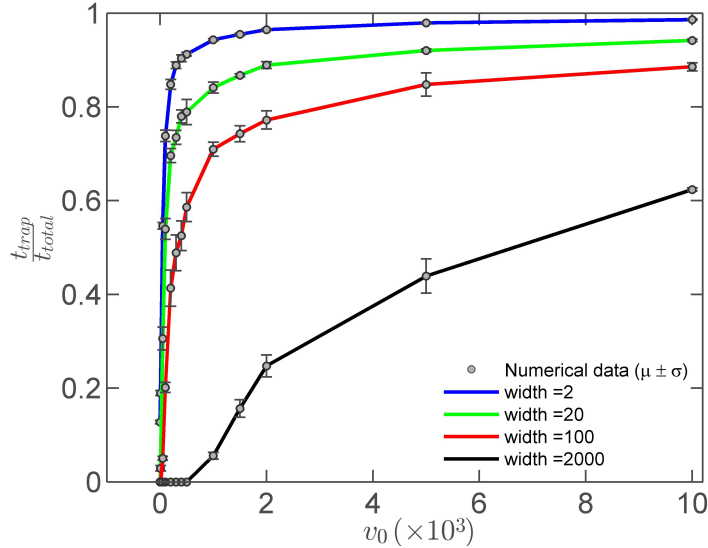


Figure 4.19: Relative trapping time at the boundaries as a function of the strength of the self-propelled velocity for different values of channels width. For a very large width, and low v_0 , the relative trapping time becomes 0 (see black curve) since the particle never reaches the boundary. $D = 1$, $D_{rot} = 0.5$, simulation time = 10 s.

4.4.2 Trapping time as a function the rotational diffusion constant

Figure 4.20 shows the trapping time as a function of the rotational diffusion constant D_{rot} for different values of the translational diffusion constant D . Two limit cases can be considered: $D_{rot} \rightarrow 0$ and $D_{rot} \rightarrow \infty$. When D_{rot} approaches 0, the direction of self-propulsion will not change. The only way for a particle to avoid collision with the boundary using a simulation time of 100 s, a self-propelled strength $v_0 = 20$ and channel width equal to 200, is to have its direction of self-propulsion very close parallel to the x-axis and having a low translational diffusion constant that will not be able to kick the particle towards the boundary in the given simulation time. It is clear that the contribution from particles that have their self-propelling component lying in this narrow range is very small. The other particles that will reach the boundary, will only detach if a Brownian kick is large enough to overcome the self-propelling contribution. Such a sufficiently large enough kick can occur for any diffusion constant, since the strength of the kicks is Gaussian distributed, but a kick large enough to detach the particle will be less likely as D decreases. In Figure 4.20, the trapping time indeed decreases when D is increased. The relative trapping time for D_{rot} going to zero reaches a value that will depend on v_0 , D and the channel's width. When $D_{rot} \rightarrow \infty$, the relative trapping time becomes independent of D_{rot} , this is because if D_{rot} is sufficiently large, a random orientation will be picked at every time step in the interval $[0, 2\pi]$, increasing D_{rot} will just do the same, i.e. picking a random orientation from $[0, 2\pi]$. The constant function it will become, depends just as the other limit case on v_0 , D and the channel's width.

The results presented in Figure 4.20 demonstrate that the “directional locking” [9] of the motion of Janus particles is an efficient mechanism of the enhancement of the trapping time. Indeed, suppressing the rotational diffusion below the value $D_{rot} < 0.5$ provides a significant increase in the trapping time, i.e., when fluctuations in the orientation of the active swimmers are insufficient to change the direction of self-propulsion (guided by the boundary), the effect being useful for the applications.

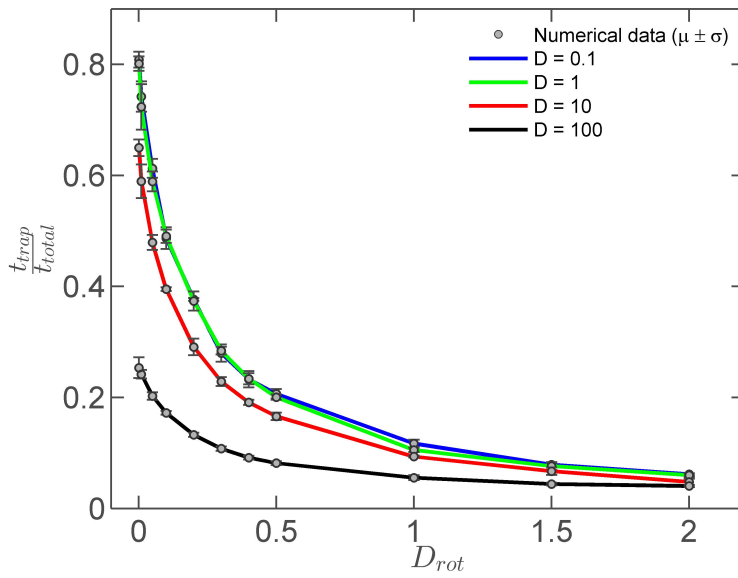


Figure 4.20: Relative trapping time as a function of the rotational diffusion constant D_{rot} for different values of the translational diffusion constant D . $D = 0.1$, simulation time=100 s, width=200 and $v_0=20$.

Figure 4.21 shows the relative trapping time as a function of the rotational diffusion constant D_{rot} for different widths of the channel. Of course as the channels width decreases, the relative trapping time will decrease. When the channel's width increases, a smaller width will decrease the relative trapping time and the effect of D_{rot} becomes smaller (see blue curve in Figure 4.21).

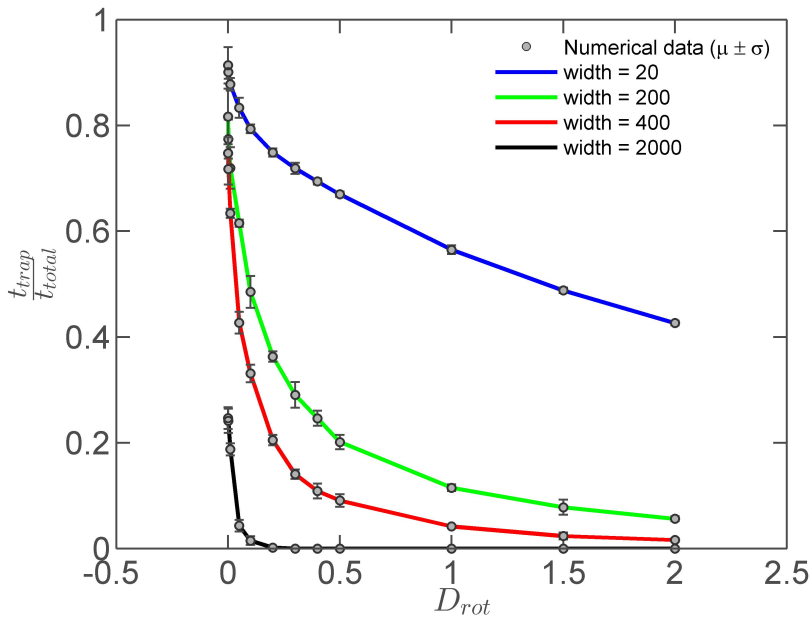


Figure 4.21: Relative trapping time as a function of the rotational diffusion constant D_{rot} for different values of the channel's width. $D = 1$, simulation time=25 s, $v_0 = 20$, channel's width=2.

4.4.3 Depletion force at the boundary

Suspensions of colloidal particles in a solvent include objects of different length scales: the colloidal particles, typical 100 nm or more and the smaller solvent molecules, typical a fraction of a nanometer. The pressure of the smaller molecules give rise to an attractive force between the colloids. A basic example to illustrate this effect is a system that consists of two parallel plates immersed in a liquid. When the distance d between the two parallel plates is less than the diameter of the fluid molecules, $d < 2R_{fluid}$, these molecules will be expelled from the gap between the plates, this is illustrated in Figure 4.22. The depletion of fluid molecules in the space between the two plates leads to the anisotropy of the local pressure gradient around the plates which will induce the attractive depletion force between the plates. This effect was first predicted by Oosawa and Asakure [50], [51]. They showed that the net force acting on the plates is equal to the pressure of the surrounding gas/liquid.

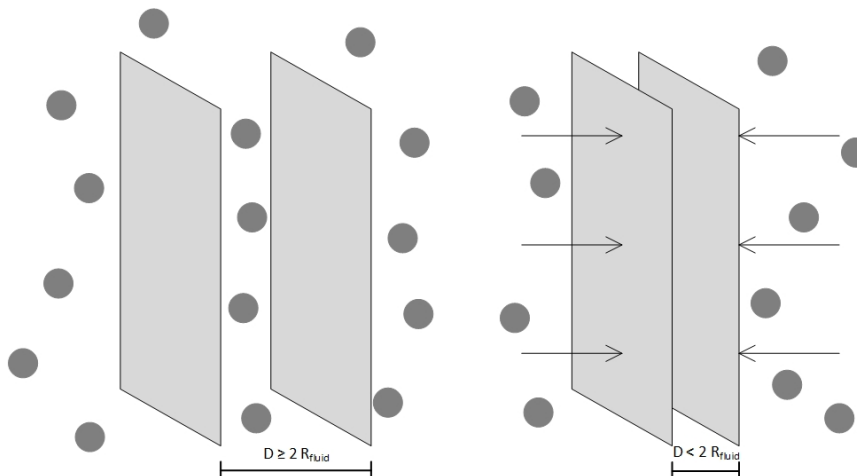


Figure 4.22: A depletion force occurs when the distance between the two plates is smaller than the radius of the fluid particles. The effective force is equal to the pressure to the surrounding fluid.

A similar effect can take place when a particle is in contact with the boundary. In theory, a spherical particle will touch the boundary in a single point. In the area between the boundary and the particle solute molecules can enter and give rise to the detachment of the particle from the boundary. The area from which particles can not enter further will be called the **shadow area**. Figure 4.23 schematically illustrates the situation: the solute particles will not be able to enter indefinitely in between the space of the colloid and the boundary.

In this subsection the relative trapping time of active particles at the boundary will be studied as a function of this shadow area.

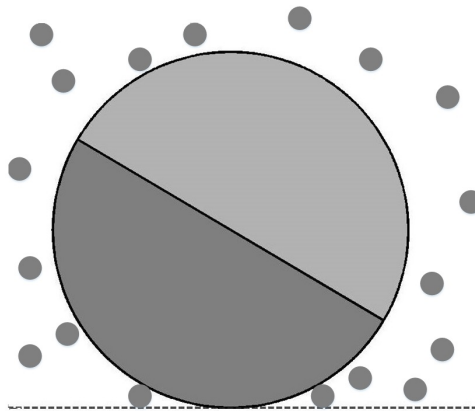
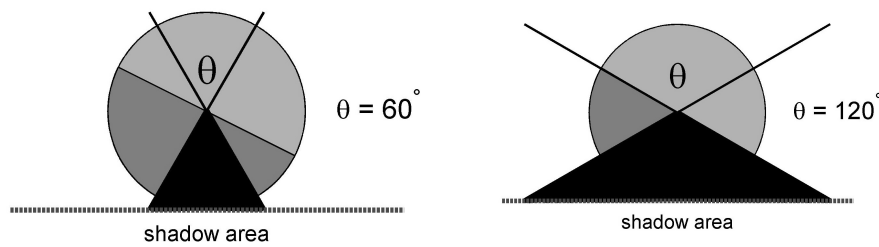


Figure 4.23: There is a maximum position to where the solute molecules can enter the space between the boundary and the colloid, this is schematically shown by two solute molecules at the bottom of the bigger colloid.

Since only symmetrical particles are considered, the shadow area can be defined with one angle θ , this angle will be called the **shadow angle**. This angle is defined as the top angle of the triangle that can be constructed by connecting the center of the particle with the maximum positions from where a solute particle can enter. Figure 4.24 illustrates how the shadow angle θ determines the shadow area. The 4.24 (a) shows a shadow area that illustrates with a angle $\theta = 30^\circ$ and Figure 4.24 (b) shows a shadow area that corresponds with $\theta = 60^\circ$. The greater the angle, the greater the shadow area and thus the less likely that a particle will be able to detach from the boundary. In the limit $\theta = 90^\circ$, the particle will not detach from the boundary due to Brownian motion. The only way for this particle to detach is to wait for the self-propelled component to be turned away from the boundary.



(a) A Self-propelled particle trapped by the boundary that has a shadow angle $\theta = 30^\circ$

(b) A Self-propelled particle trapped by the boundary that has a shadow angle $\theta = 60^\circ$.

Figure 4.24

Figure 4.25 shows the relative trapping time as a function of the shadow angle θ for different widths of the channel. As the shadow angle increases, the trapping time increases for all displayed widths. The effect is smaller for small and large widths. This is because both cases approach the limit cases where the trapping time is going to 1 for a width going to 0 and a trapping time going to 0 for a width that is large enough, so it never will be trapped by the boundary.

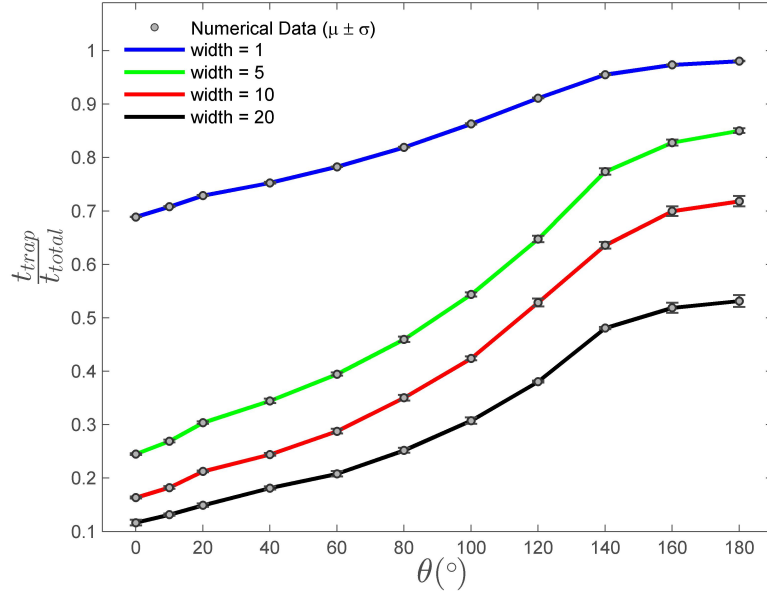


Figure 4.25: Relative trapping time as a function of the shadow angle for different widths of the channel. The other parameters are: $D = 5$, $D_{rot}=0.05$, $v_0 = 2$, simulation time=25 s.

Figure 4.26 shows again the relative trapping time as a function of the shadow angle, but now for different D_{rot} . For a low rotational diffusion constant, the depletion force will play a bigger role than for larger constants. This is because as the shadow angle increases (and thus the depletion force), D_{rot} becomes the only way for a particle to detach from the boundary: the particle has to "wait" for its self-propelled component to turn away from the boundary. The lower D_{rot} , the longer this will take. For high D_{rot} , the trapping time will become independent of the shadow angle as the particle self-propulsion will resemble normal Brownian motion for high D_{rot} .

Figure 4.27 shows what happens for different v_0 . As v_0 becomes very high, it will be impossible to escape the boundary when $\theta = 90^\circ$. This is illustrated by the black curve.

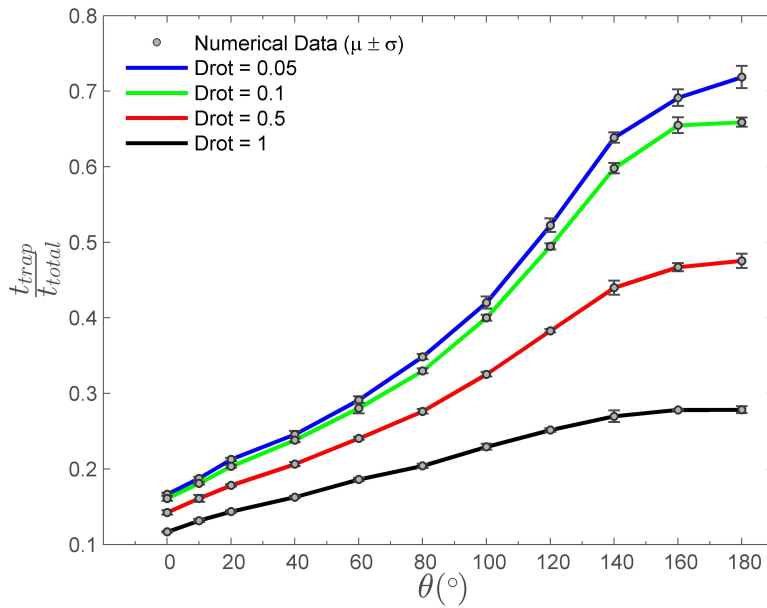


Figure 4.26: Relative trapping time as a function of the shadow angle for different D_{rot} . The other parameters for this figure are: $D = 5$, width = 10, $v_0 = 2$, simulation time=25 s.

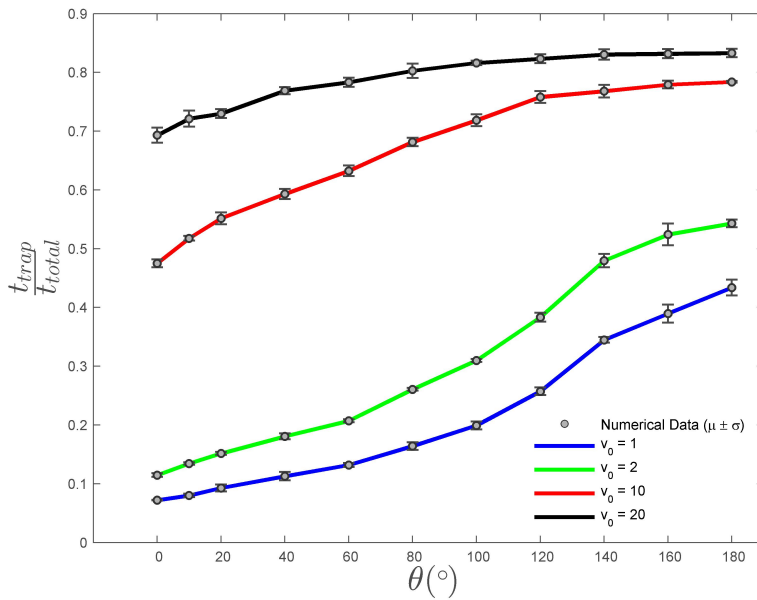


Figure 4.27: Relative trapping time as a function of the shadow angle for different v_0 . The other parameters for this figure are: $D = 5$, $D_{rot}=0.05$, width = 10, simulation time=25 s.

This analysis shows that, together with the suppression of the rotational noise, the depletion interaction could provide an important contribution to the increase of the trapping time. The depletion interaction could also be a reason, together with other possible mechanisms (such as, e.g., electrostatic interaction), of the short-range interaction between Janus particles and passive colloids and between Janus particles and the boundaries, as observed in the experiment [9] where this attraction was treated as an “effective” attractive term in the inter-particle interaction. The results of this section provide a somewhat detailed analysis of the depletion-interaction contribution to the effective attraction.

Chapter 5

Conclusions

The first step of the presented research was devoted to the demonstration of the capability of the developed numerical procedures to reproduce known experimental and theoretical results. First, simulations were able to reproduce experimental and theoretical MSD curves for Brownian motion. The effect of sliding & reflecting boundaries on the MSD was found to result in a different long-time diffusion constant (than for a free particle), this constant was roughly half of the constant without boundaries. This is in line with the expectations: indeed a dimensional restriction $(d - 1)|_{d=2}$ will result in a new diffusion constant $D_{new} = \frac{1}{2}D$. Next, a good agreement with the theoretical MSD for single diffusion (SFD) was obtained by using soft-core Brownian particles. Built on these results, long-time exponents for different widths of a narrow channel were found, these were in the range $0.5 < \alpha < 1$. For active particles, the effect of sliding and reflecting boundaries was found to facilitate a faster crossover to a regime where $MSD \propto t^\alpha, \alpha = 1$. Although this effect was found to be rather small, and a very small difference between reflecting and sliding boundaries was also found. Clustering of active particles is observed for low density and higher density. For a lower density, the particles reside more along the boundary whilst for higher density, more particles are starting to get trapped between the layer formed at the boundary. No effect of sliding or reflecting boundary conditions was found. However, for random boundary conditions, a much more homogeneous distribution of the particles was observed. Clusters were observed to still form, but these were rather fast destroyed. These observations are also in a good agreement with known literature.

In the last chapter, new original results were presented regarding the trapping time of active particles at the boundary. The trapping time was defined as the relative time a particle being resided in the vicinity of the boundary, to the total observation time. An algorithm was developed to identify and calculate this trapping time. This trapping time is examined as a function of various parameters, i.e., the diffusion constant D , the rotational diffusion constant D_{rot} , the self-propelled velocity v_0 and the channels width. It could be important for future applications to require a specific trapping time at the boundary whilst, for example, be restricted in the use of a certain width, the results provided here can give insights in how to achieve this time whilst some parameters may be restricted.

More specifically, in relation to experiments with self-propelled particles in narrow channels, one important conclusion of this work is that, for

a wide range of the diffusion constants typical for experiments, i.e., ranging from $D = 0.001$ to 10 , even moderate values of the self-propelled velocity, $v_0 \approx 2 \mu\text{m}^{-1}$, provide relatively high values of the trapping time, $t_{trap} > 0.7$. Also, it is worth noticing that the function $t_{trap}(v_0)$ shows a saturation for the values of the diffusion constant lower than $D = 10$, i.e., the value of $D = 10$ is a sufficient lower bound that provides a fast increase of t_{trap} with increasing v_0 .

On the other hand, the obtained dependences of the trapping time on the rotational diffusion demonstrate that the “directional locking” of the motion of Janus particles is an efficient mechanism of the enhancement of the trapping time. As follows from the results presented in this work, suppressing the rotational diffusion below the value $D_{rot} < 0.5$ provides a significant increase in the trapping time, i.e., when fluctuations in the orientation of the active swimmers are insufficient to change the direction of self-propulsion (guided by the boundary), the effect being useful for the applications.

Lastly, a depletion force was considered for active particles near the boundary, this force is especially important for particles with a low rotational diffusion constant and a large self-propelled velocity. Experimentalists that are concerned with particles being as long at the boundary as possible could be interested in using solutions with solute molecules that are larger in order to facilitate a greater depletion force.

The analysis of the depletion interaction shows that, together with the suppression of the rotational noise, this interaction provides an important contribution to the increase of the trapping time. The depletion interaction could also be a reason, together with other possible mechanisms (such as, e.g., electrostatic interaction), of the short-range interaction between Janus particles and passive colloids and between Janus particles and the boundaries, as observed in the experiments.

Bibliography

1. Costanzo, A, Leonardo, R. D., Ruocco, G & Angelani, L. Transport of self-propelling bacteria in micro-channel flow. *Journal of Physics: Condensed Matter* **24**, 065101 (2012).
2. Muddana, H. S., Sengupta, S., Mallouk, T. E., Sen, A. & Butler, P. J. Substrate Catalysis Enhances Single-Enzyme Diffusion. *Journal of the American Chemical Society* **132**. PMID: 20108965, 2110–2111 (2010).
3. Ebbens, S. J. & Howse, J. R. In pursuit of propulsion at the nanoscale. *Soft Matter* **6**, 726–738 (4 2010).
4. Yuan, Y. *et al.* Nanoparticle delivery of anticancer drugs overcomes multidrug resistance in breast cancer. *Drug Delivery* **23**. PMID: 27098896, 3350–3357 (2016).
5. Baylis, J. R. *et al.* Self-propelled particles that transport cargo through flowing blood and halt hemorrhage. **1** (2015).
6. Jain, R. K. & Stylianopoulos, T. Delivering nanomedicine to solid tumors. *Nature Reviews Clinical Oncology* **7**, 653–664 (2010).
7. Wang, A., Langer, R. & Farokhzad, O. Nanoparticle delivery of cancer drugs. *Annual Review of Medicine* **63**, 185–198. ISSN: 0066-4219 (2012).
8. Balasubramanian, S. *et al.* Cover Picture: Micromachine-Enabled Capture and Isolation of Cancer Cells in Complex Media (Angew. Chem. Int. Ed. 18/2011). *Angewandte Chemie International Edition* **50**, 4023–4023 (2011).
9. Yu, H. *et al.* Confined Catalytic Janus Swimmers in a Crowded Channel: Geometry-Driven Rectification Transients and Directional Locking. *Small* **12**, 5882–5890. ISSN: 1613-6829 (2016).
10. Schliwa, M. & Woehlke, G. Molecular motors. *Nature* **422**, 759–765 (2003).
11. Moran, J. L. & Posner, J. D. Phoretic Self-Propulsion. *Annual Review of Fluid Mechanics* **49**, 511–540 (2017).
12. Anderson, J. L. Colloid Transport by Interfacial Forces. *Annual Review of Fluid Mechanics* **21**, 61–99 (1989).
13. Paxton, W. F. *et al.* Catalytic Nanomotors: Autonomous Movement of Striped Nanorods. *ChemInform* **35** (2004).
14. Wang, Y. *et al.* Bipolar Electrochemical Mechanism for the Propulsion of Catalytic Nanomotors in Hydrogen Peroxide Solutions. *Langmuir* **22**. PMID: 17129015, 10451–10456 (2006).
15. Moran, J. L., Wheat, P. M. & Posner, J. D. Locomotion of electrocatalytic nanomotors due to reaction induced charge autoelectrophoresis. *Phys. Rev. E* **81**, 065302 (6 2010).
16. Ismagilov, R. F., Schwartz, A., Bowden, N. & Whitesides, G. M. Autonomous Movement and Self-Assembly. *Angewandte Chemie* **114**, 674–676 (2002).

17. Jiang, H.-R., Yoshinaga, N. & Sano, M. Active Motion of a Janus Particle by Self-Thermophoresis in a Defocused Laser Beam. *Phys. Rev. Lett.* **105**, 268302 (26 2010).
18. Würger, A. Thermophoresis in Colloidal Suspensions Driven by Marangoni Forces. *Phys. Rev. Lett.* **98**, 138301 (13 2007).
19. Parola, A. & Piazza, R. A microscopic approach to thermophoresis in colloidal suspensions. *Journal of Physics: Condensed Matter* **17**, S3639 (2005).
20. Lobaskin, V., Lobaskin, D. & Kulic, I. M. Brownian dynamics of a microswimmer. *The European Physical Journal Special Topics* **157**, 149–156 (2008).
21. Erdmann, U., Ebeling, W. & Anishchenko, V. S. Excitation of rotational modes in two-dimensional systems of driven Brownian particles. *Phys. Rev. E* **65**, 061106 (6 2002).
22. Peruani, F. & Morelli, L. G. Self-Propelled Particles with Fluctuating Speed and Direction of Motion in Two Dimensions. *Phys. Rev. Lett.* **99**, 010602 (1 2007).
23. Howse, J. R. *et al.* Self-Motile Colloidal Particles: From Directed Propulsion to Random Walk. *Phys. Rev. Lett.* **99**, 048102 (4 2007).
24. Simmchen, J. *et al.* Topographical pathways guide chemical microswimmers. *Nature Communications* **7**, 10598 (2016).
25. Khalil, I. S. M., Magdanz, V., Sanchez, S., Schmidt, O. G. & Misra, S. Precise Localization and Control of Catalytic Janus Micromotors Using Weak Magnetic Fields. *International Journal of Advanced Robotic Systems* **12**, 2 (2015).
26. Baraban, L. *et al.* Catalytic Janus Motors on Microfluidic Chip: Deterministic Motion for Targeted Cargo Delivery. *ACS Nano* **6**. PMID: 22424213, 3383–3389 (2012).
27. Baraban, L. *et al.* Control over Janus micromotors by the strength of a magnetic field. *Nanoscale* **5**, 1332–1336 (4 2013).
28. Gangwal, S., Cayre, O. J. & Velev, O. D. Dielectrophoretic Assembly of Metallodielectric Janus Particles in AC Electric Fields. *Langmuir* **24**, 13312–13320 (2008).
29. Campbell, A. I. & Ebbens, S. J. Gravitaxis in Spherical Janus Swimming Devices. *Langmuir* **29**, 14066–14073 (2013).
30. Spagnolie, S. E. & Lauga, E. Hydrodynamics of self-propulsion near a boundary: predictions and accuracy of far-field approximations. *Journal of Fluid Mechanics* **700**, 105–147 (2012).
31. Volpe, G., Buttinoni, I., Vogt, D., Kummerer, H.-J. & Bechinger, C. Microswimmers in patterned environments. *Soft Matter* **7**, 8810–8815 (19 2011).
32. Das, S. *et al.* Boundaries can steer active Janus spheres. *Nature Communications* **6**, 8999+. ISSN: 2041-1723 (Dec. 2015).
33. Astumian, R. D. Adiabatic Pumping Mechanism for Ion Motive ATPases. *Phys. Rev. Lett.* **91**, 118102 (11 2003).

34. Roth, R. & Gillespie, D. Physics of Size Selectivity. *Phys. Rev. Lett.* **95**, 247801 (24 2005).
35. Doyle, P. S., Bibette, J., Bancaud, A. & Viovy, J.-L. Self-Assembled Magnetic Matrices for DNA Separation Chips. *Science* **295**, 2237–2237. ISSN: 0036-8075 (2002).
36. He, Y. *et al.* Tuning Transport Properties of Nanofluidic Devices with Local Charge Inversion. *Journal of the American Chemical Society* **131**. PMID: 19317490, 5194–5202 (2009).
37. Ghosh, P. K., Misko, V. R., Marchesoni, F. & Nori, F. Self-Propelled Janus Particles in a Ratchet: Numerical Simulations. *Phys. Rev. Lett.* **110**, 268301 (26 2013).
38. Guidobaldi, A. *et al.* Geometrical guidance and trapping transition of human sperm cells. *Phys. Rev. E* **89**, 032720 (3 2014).
39. Ghosh, P. K. Communication: Escape kinetics of self-propelled Janus particles from a cavity: Numerical simulations. *The Journal of Chemical Physics* **141**, 061102 (2014).
40. MATLAB. *version 8.1.0.604 (R2013a)* (The MathWorks Inc., Natick, Massachusetts, 2013).
41. Hodgkin, A. L. & Keynes, R. D. The potassium permeability of a giant nerve fibre. *The Journal of Physiology* **128**, 61–88 (1955).
42. Lebowitz, J. L. & Percus, J. K. Kinetic Equations and Density Expansions: Exactly Solvable One-Dimensional System. *Physical Review* **155**, 122–138 (1967).
43. Alexander, S. & Pincus, P. Diffusion of labeled particles on one-dimensional chains. *Phys. Rev. B* **18**, 2011–2012 (4 1978).
44. Kärger, J. Straightforward derivation of the long-time limit of the mean-square displacement in one-dimensional diffusion. *Phys. Rev. A* **45**, 4173–4174 (6 1992).
45. Nelissen, K., Misko, V. R. & Peeters, F. M. Single-file diffusion of interacting particles in a one-dimensional channel. *EPL (Europhysics Letters)* **80**, 56004 (2007).
46. Lucena, D. *et al.* Transition from single-file to two-dimensional diffusion of interacting particles in a quasi-one-dimensional channel. *Phys. Rev. E* **85**, 031147 (3 2012).
47. Claessen, T. *Video 1: low rotational diffusion constant* 2017. <<https://youtu.be/2AQ61Q19WJk>>.
48. Claessen, T. *Video 2: high rotational diffusion constant* 2017. <<https://youtu.be/L6ED0d8G1M8>>.
49. Blaschke, J., Maurer, M., Menon, K., Zöttl, A. & Stark, H. Phase separation and coexistence of hydrodynamically interacting microswimmers. *Soft Matter* **12**, 9821–9831 (2016).
50. Oosawa, F. & Asakura, S. Surface Tension of High-Polymer Solutions. *The Journal of Chemical Physics* **22**, 1255–1255 (1954).
51. Asakura, S. & Oosawa, F. Interaction between particles suspended in solutions of macromolecules. *Journal of Polymer Science* **33**, 183–192. ISSN: 1542-6238 (1958).